J. Fluid Mech. (2008), *vol.* 604, *pp.* 411–445.
doi:10.1017/S0022112008001341 Printed in the United Kingdom

Linear stability analysis of pressure-driven flows in channels with porous walls

NILS TILTON AND LUCA CORTELEZZI†

Department of Mechanical Engineering, McGill University, Montreal, Quebec H3A 2K6, Canada

(Received 31 May 2007 and in revised form 28 February 2008)

We present the three-dimensional linear stability analysis of a pressure-driven, incompressible, fully developed, laminar flow in a channel delimited by rigid, homogeneous, isotropic, porous layers. We consider porous materials of small permeability in which the maximum fluid velocity is small compared to the mean velocity in the channel region and for which inertial effects may be neglected. We analyse the linear stability of symmetric laminar velocity profiles in channels with two identical porous walls as well as skewed laminar velocity profiles in channels with only one porous wall. We solve the fully coupled linear stability problem, arising from the adjacent channel and porous flows, using a spectral collocation technique. We validate our results by recovering the linear stability results of a flow in a channel with impermeable walls as the permeabilities of the porous layers tend to zero. We also verify that our results are consistent with the assumption of negligible inertial effects in the porous regions. We characterize the stability of pressure-driven flows by performing a parametric study in which we vary the permeability, porosity, and height of the porous layers as well as an interface coefficient, τ, associated with the momentum transfer process at the interfaces between the channel and porous regions. We find that very small amounts of wall permeability significantly affect the Orr–Sommerfeld spectrum and can dramatically decrease the stability of the channel flow. Within our assumptions, in channels with two porous walls, permeability destabilizes up to two Orr–Sommerfeld wall modes and introduces two new damped wall modes on the left branch of the spectrum. In channels with only one porous wall, permeability destabilizes up to one wall mode and introduces one new damped wall mode on the left branch of the spectrum. In both cases, permeability also introduces a new class of damped modes associated with the porous regions. The size of the unstable region delimited by the neutral curve grows substantially, and the critical Reynolds number can decrease to only 10 % of the corresponding value for a channel flow with impermeable walls. We conclude our study by considering two real materials: foametal and aloxite. We fit the porosity and interface coefficient τ to published data so that the porous materials we model behave like foametal and aloxite, and we compare our results with previously published numerical and experimental results.

1. Introduction

This study is motivated by the extensive use of wall permeability and transpiration in studies of such diverse fields as filtration, papermaking, transpiration cooling, aeronautics, the inhibition of wall turbulence, aquatic biology, flows through geological

† Author to whom correspondence should be addressed: crtlz@cim.mcgill.ca.

media, and biomechanics. As examples, we cite studies in industrial crossflow filtration systems (Nassehi 1998); transpiration cooling of rocket engines and gas turbine blades (Jiang *et al.* 2004); the use of wall suction to delay transition to turbulence over the surface of a wing (Joslin 1998); fluid transport in blood vessels, the gastrointestinal system, kidneys, and lungs where mass transfer between air, blood, and tissue occurs at the walls (Majdalani, Zhou & Dawson 2002; Chang *et al.* 1989); sediment–water interfaces over permeable seabeds (Goharzadeh, Khalili & Jørgensen 2005); and flow through fractured geological formations (Berkowitz 2002).

Schlichting (see Schlichting & Gersten 2000) and Berman (1953) first modelled the influence of continuous wall suction and blowing on boundary layers and channel flows, respectively, by prescribing a continuous wall-normal velocity and simultaneously enforcing the no-slip condition. While this approach is now rarely used in the porous flow community, where there has been considerable work on fluid flows adjacent to porous media (see Ochoa-Tapia & Whitaker S. 1995*a*; Alazmi & Vafai 2001; Shavit, Rosenzweig & Assouline 2004), it remains common in the hydrodynamic stability and flow control community where most work assumes that the flow inside the porous walls and the effects of the porous walls on the tangential velocity at the interfaces are negligible. One promising method of inhibiting wall turbulence, for example, supposes that one could line the walls of a channel with small pores. The pores inject and remove fluid in a coordinated effort to attenuate wall disturbances in order to inhibit transition to turbulence or reduce skin-friction drag in fully developed turbulent flows. Encouraging computer-simulated results have been obtained when the pores are assumed to be sufficiently small and densely packed to allow the design of controllers able to coordinate a continuously distributed actuation at the walls (Kim 2003).

To the best of our knowledge, numerical investigations of boundary layer control using the above method of actuation assume that the no-slip condition is satisfied at the porous wall. While this assumption makes the numerical implementation of the problem feasible, it is not clear that an actuated surface behaves like a solid boundary when it is made of small, but finite, densely distributed pores. The no-slip assumption may be non-physical because flows above porous walls generally have a non-zero tangential velocity at the interface (Beavers & Joseph 1967). Furthermore, there is experimental (Sparrow *et al.* 1973) and analytical evidence (Sparrow *et al.* 1973; Tilton & Cortelezzi 2006) that wall permeability can dramatically destabilize channel flows in comparison to flows in channels with impermeable walls.

In order to put our study in perspective, we briefly outline previous pertinent work on porous flows. In 1856, Darcy (see Lage 1998) developed the first empirical law governing Stokes flow through porous media. Beavers & Joseph (1967) proposed the first interface condition coupling a fully developed laminar channel flow with an adjacent porous flow governed by Darcy's law. Because Darcy's law cannot resolve boundary layers, the condition results in a velocity discontinuity at the interface. Whitaker (1996) analytically derived general porous flow equations by volume averaging the Navier–Stokes and continuity equations. Finally, Ochoa-Tapia & Whitaker (1995*a*, *b*, 1998) analytically derived interfacial momentum transfer conditions which couple a homogeneous fluid flow with an adjacent porous flow.

To the best of our knowledge, Beavers, Sparrow & Magnuson (1970) were the first to report the destabilizing effects of wall permeability experimentally. Subsequently, Sparrow *et al.* (1973) experimentally determined a few critical Reynolds numbers in a channel with one porous wall, and performed a two-dimensional linear stability analysis using Darcy's law with the Beavers & Joseph (1967) interface condition.

They found, both experimentally and numerically, that wall permeability decreased the critical Reynolds number with respect to the value for a flow in a channel with impermeable walls. More recently, Tilton & Cortelezzi (2006) performed a three-dimensional linear stability analysis of a laminar flow in a channel with two identical, homogeneous, isotropic, porous walls by modelling the flow in the porous walls using the governing equations of Whitaker (1996) with the interface conditions of Ochoa-Tapia & Whitaker (1995*a*). Tilton & Cortelezzi (2006) found that very small amounts of wall permeability can dramatically decrease the stability of channel flows with respect to channel flows with impermeable walls.

A thorough literature review of coupled channel flows and porous flows reveals inconsistencies in the usage of the proper governing equations in the porous regions and the interface conditions which couple the flow in porous regions to the flow in the channel region. Tilton & Cortelezzi (2006) noted two recently published linear stability analyses which claim to include inertial effects in porous regions without properly accounting for these effects in the governing equations and interface conditions. More recently, Chang, Chen & Straughan (2006) considered the linear stability of a channel flow with one porous wall by modelling the flow in the porous region using Darcy's law with the Beavers & Joseph (1967) interface condition. While this model is valid if inertial effects are negligible in the porous region, Chang *et al.* (2006) only considered porous materials for which this not a good assumption. The current study attempts to correct some of the misinterpretations of the governing equations and interface conditions as well as provide a solid springboard for investigating the stability of flows in the presence of interfaces with high-permeability porous materials.

In this study, we considerably extend and generalize the work by Tilton & Cortelezzi (2006). The latter work considered a channel with two identical porous walls. The porosity and height of the porous layers, as well as an interface coefficient, τ, associated with the momentum transfer process at the interfaces between the channel and porous regions, were fixed and only the permeability was varied. In the current study, we analyse the linear stability of symmetric laminar velocity profiles in channels with two identical porous walls, as well as skewed laminar velocity profiles in channels with only one porous wall or two porous walls of differing permeability. We also characterize the stability of pressure-driven flows by performing a parametric study in which we vary the permeability, porosity, the height of the porous layers, and the coefficient τ. Furthermore, we present the effects of wall permeability on both the Orr–Sommerfeld and Squire modes. We find that the effects of small wall permeability on the linear stability of channel flows is far richer and more complicated than previously observed by Tilton & Cortelezzi (2006), and the overall stability of a channel with porous walls is dictated by several competing mechanisms. Due to the presence of the porous walls, there is a non-zero tangential and normal velocity at the interfaces between the channel and the porous layers. By varying the height of the porous layers, we find that the presence of a normal velocity is destabilizing. By varying the interface coefficient, τ, we find that the presence of a tangential velocity is stabilizing. By considering channels with only one porous wall or two porous walls of differing permeability, we find that the presence of a non-symmetric laminar velocity profile has a stabilizing effect. As in the work of Tilton & Cortelezzi (2006), we solve the fully coupled linear stability problem, arising from the adjacent channel and porous flows, using a spectral collocation technique, and we validate our results by recovering the linear stability results of a flow in a channel with impermeable walls as the permeabilities of the porous layers tend to zero. We also verify that our results are consistent with the assumption of negligible inertial effects in the porous regions. We conclude our

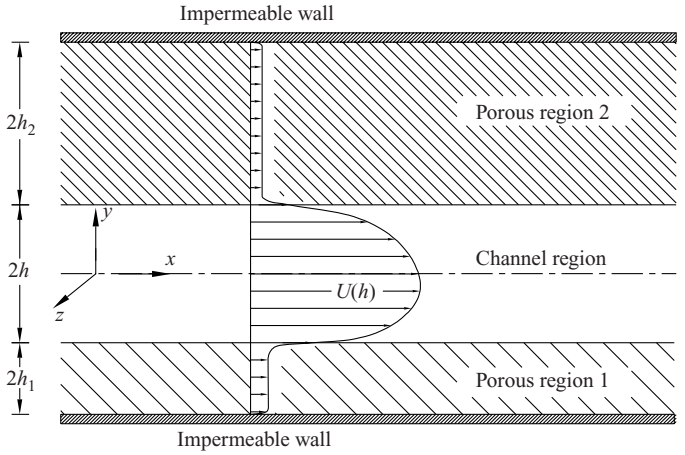

FIGURE 1. The channel geometry and laminar profile, not to scale, considered in this study.

study by considering two real materials: foametal and aloxite. We fit the porosity and interface coefficient τ to published data so that the porous materials we model behave like foametal and aloxite, and we compare our results with those of Sparrow *et al.* (1973) and Chang *et al.* (2006).

We have organized this article as follows. In § 2, we describe the channel geometry and discuss and justify our choice of governing equations and interface conditions. In § 3, we derive a general analytical expression for the laminar profile. In § 4, we non-dimensionalize the problem and derive the linear stability equations and interface conditions. In § 5, we illustrate the numerical solution of the coupled problem. In § 6, we present the results for the linear stability of symmetric laminar velocity profiles in channels with two identical porous walls. In § 7, we present the results for skewed laminar velocity profiles in channels with only one porous wall or two porous walls of differing permeability and compare our results with those of Sparrow *et al.* (1973) and Chang *et al.* (2006). Finally, we summarize our conclusions in § 8.

2. Governing equations

Figure 1 illustrates the channel geometry used in this study. The channel is delimited by parallel, rigid, homogeneous, isotropic, porous layers sealed by impermeable walls. We define the channel height as $2h$ and the height of the lower and upper porous layers as $2h_1$ and $2h_2$, respectively, because it simplifies the numerical solution of the coupled linear stability problem. A uniform pressure gradient, $\mathrm{d}p/\mathrm{d}x$, drives a fully developed, laminar, incompressible flow, $u(y)$, in the longitudinal direction only, in both the channel region and the porous layers. The two porous layers do not necessarily have the same properties or thicknesses, and in general, the laminar flow in the channel region is skewed toward the porous region with larger interface velocity. By setting the permeability of both porous regions to zero, we recover the linear stability results for a flow in a channel with impermeable walls. By setting the permeability of only one porous region to zero, we compare our results with those of Sparrow *et al.* (1973) and Chang *et al.* (2006).

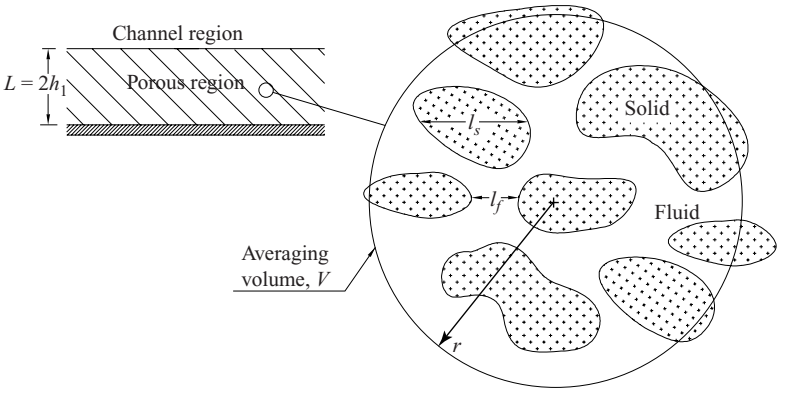

FIGURE 2. Sketch of a porous medium with complicated fluid–solid interfaces and a wide range of length scales. Not to scale.

2.1. *The governing equations for the channel region*

The flow of an incompressible viscous fluid in the channel region of figure 1 is governed by the Navier–Stokes and continuity equations,

$$\rho\left(\frac{\partial \boldsymbol{v}}{\partial t} + \boldsymbol{v}\cdot\nabla\boldsymbol{v}\right) = -\nabla p + \mu\nabla^2\boldsymbol{v}, \tag{2.1}$$

$$\nabla\cdot\boldsymbol{v} = 0, \tag{2.2}$$

where $\boldsymbol{v} = [u\ v\ w]^T$, p, ρ, and μ, are the fluid velocity vector, pressure, density, and viscosity, respectively.

2.2. *The governing equations for the porous regions and interface conditions*

The flow of an incompressible viscous fluid through a porous medium is also governed by the Navier–Stokes and continuity equations (2.1) and (2.2) with no-penetration and no-slip conditions at the fluid–solid interfaces: see figure 2. Two common forms of porous media are sponge-like porous foams, such as foametals, and porous beds of packed particles, such as sand, gravel and aloxite. Solving the boundary value problem governed by (2.1) and (2.2) is often prohibitively difficult because porous media generally involve a wide range of length scales and have extremely complex boundary conditions. The smallest length scales, l_f and l_s, are generally on the order of an average pore and particle diameter, respectively, while the largest length scale, L, is the characteristic macroscopic length of the porous medium: see figure 2. In this study, for example, the macroscopic length scale, L, of the lower porous region is the thickness of the porous layer, e.g. $2h_1$.

The method of volume averaging simplifies the problem by considering only the large-scale behaviour of the flow in the porous regions, which is often referred to as the *macroscopic* behaviour. This is done by averaging the governing equations over a small volume, V, of radius $r \ll L$, and solving for volume-averaged values of the velocity and pressure fields, see figure 2. In general, the length scales are assumed to be well separated, i.e. $l_s \sim l_f \ll r \ll L$. Whitaker (1986) notes that the radius r should be large enough so that volume-averaged quantities result in smooth functions that are free of small-scale fluctuations. Because volume-averaged quantities are associated with the centroid of the averaging volume, V, every point in a volume-averaged flow field, even a point within the solid, has a volume-averaged velocity associated with it, and the porous medium is treated as a continuum.

To identify the two different types of averages that are used in the method of volume averaging, we adopt Whitaker's convention (Whitaker 1996) which defines the *superficial* volume average, $\langle\ \rangle$, of some function, ψ_f, associated with the fluid as

$$\langle\psi_f\rangle = \frac{1}{V}\int_{V_f}\psi_f\,\mathrm{d}V_f,$$

and defines the *intrinsic* volume average, $\langle\ \rangle^f$, as

$$\langle\psi_f\rangle^f = \frac{1}{V_f}\int_{V_f}\psi_f\,\mathrm{d}V_f,$$

where $V_f < V$ is the volume of fluid contained in the averaging volume, V. The two averages are related by $\langle\psi_f\rangle = \varepsilon\langle\psi_f\rangle^f$, where $\varepsilon = V_f/V$ is the *porosity*, or volume-fraction of the fluid. Note that the porosity varies between zero and one and is generally a function of position, $\boldsymbol{x}$, in a heterogeneous porous medium.

The volume-averaged Navier–Stokes and continuity equations derived by Whitaker (1996) for an incompressible viscous fluid flowing through a rigid, homogeneous, isotropic, porous medium are

$$\frac{\rho}{\varepsilon}\left(\frac{\partial\langle\boldsymbol{v}\rangle}{\partial t} + \frac{\langle\boldsymbol{v}\rangle\cdot\nabla\langle\boldsymbol{v}\rangle}{\varepsilon} + \nabla\cdot\langle\check{\boldsymbol{v}}\check{\boldsymbol{v}}\rangle\right) = -\nabla\langle p\rangle^f + \frac{\mu}{\varepsilon}\nabla^2\langle\boldsymbol{v}\rangle - \frac{\mu}{k}\langle\boldsymbol{v}\rangle - \frac{\mu}{k}\boldsymbol{F}\cdot\langle\boldsymbol{v}\rangle, \quad (2.3)$$

and

$$\nabla\cdot\langle\boldsymbol{v}\rangle = 0. \quad (2.4)$$

The superficial volume-averaged velocity, $\langle\boldsymbol{v}\rangle$, is the preferred representation of the velocity because it is always solenoidal, while the intrinsic volume-averaged velocity, $\langle\boldsymbol{v}\rangle^f$, is only solenoidal in the case of constant porosity. For the pressure, however, the intrinsic volume average, $\langle p\rangle^f$, is preferred because it is the pressure measured by a probe in an experimental apparatus. The permeability, k, measures the ease with which fluid flows through a porous medium. If $k=0$, the medium is impermeable, while if $k=\infty$, the medium offers no resistance. In equation (2.3), the Darcy term, $\mu\langle\boldsymbol{v}\rangle/k$, represents a volume-averaged viscous drag, while the Forchheimer term, $\mu\boldsymbol{F}\cdot\langle\boldsymbol{v}\rangle/k$, where $\boldsymbol{F}$ is a second-order tensor, represents a drag due to inertial effects. The exact form of $\boldsymbol{F}$ depends on the structure of the porous medium, but experimentally it is often found to be a linear function of the volume-averaged velocity, $\langle\boldsymbol{v}\rangle$ (Beavers, Sparrow & Rodenz 1973; Joseph, Nield & Papanicolaou 1982; Whitaker 1996; Giorgi 1997). The deviation velocity, $\check{\boldsymbol{v}}$, is the difference between the velocity, $\boldsymbol{v}$, and the volume-averaged velocity, $\langle\boldsymbol{v}\rangle$. It is important to note that volume averaging the convective term, $\rho(\boldsymbol{v}\cdot\nabla\boldsymbol{v})$, in the Navier–Stokes equation generates the terms $\rho(\langle\boldsymbol{v}\rangle\cdot\nabla\langle\boldsymbol{v}\rangle)/\varepsilon^2$, $\rho(\nabla\cdot\langle\check{\boldsymbol{v}}\check{\boldsymbol{v}}\rangle)/\varepsilon$, and $\mu\boldsymbol{F}\cdot\langle\boldsymbol{v}\rangle/k$ in equation (2.3). Whitaker (1996) found that the convective terms $\langle\boldsymbol{v}\rangle\cdot\nabla\langle\boldsymbol{v}\rangle/\varepsilon$ and $\nabla\cdot\langle\check{\boldsymbol{v}}\check{\boldsymbol{v}}\rangle$ are of the same order of magnitude and are both negligible in comparison with the dominant Forchheimer term, $\mu\boldsymbol{F}\cdot\langle\boldsymbol{v}\rangle/k$.

A thorough literature review reveals some inconsistencies in the proper form of the equations governing flow through porous media (see discussions in Whitaker 1996; Giorgi 1997; Lage 1998). Note that the Darcy drag, $\mu\langle\boldsymbol{v}\rangle/k$, and Forchheimer drag, $\mu\boldsymbol{F}\cdot\langle\boldsymbol{v}\rangle/k$, were originally observed experimentally. Several researchers have attempted to derive generalized porous flow equations by artificially inserting these volume-averaged drag terms into the Navier–Stokes equation (2.1). Lage (1998) describes the fundamental error in this method as a mismatch in dimensions. The Navier–Stokes equation deals with the velocity and pressure of small fluid

parcels, while the Darcy and Forchheimer drag terms deal with volume-averaged quantities. Generalized porous flow equations can also be derived using methods other than volume averaging (see Giorgi 1997); however, the volume-averaged method is particularly useful in coupling a channel flow to an adjacent porous region. Note that Vafai & Tien (1981) and Hsu & Cheng (1990) have used volume averaging to derive porous flow equations similar to equations (2.3) and (2.4). Without diminishing the importance of their work, we prefer the derivation of Whitaker (1996) because it is, to the best of our knowledge, the most complete and formal.

Equations (2.3) and (2.4) are not valid in a small heterogeneous transition layer adjacent to the interface with the channel region. In the transition layer, the structure of a porous medium undergoes rapid changes. Ochoa-Tapia & Whitaker (1995*a*, 1998), however, have derived momentum transfer conditions which use equations (2.3) and (2.4) in the transition layer and correct for the error using a jump condition in the shear stress. When inertial effects are non-negligible in the transition layer, these conditions are quite complex and involve a vector and fourth-order tensor which must both be determined experimentally (see Ochoa-Tapia & Whitaker 1998).

Because there are currently no published data for these quantities, we restrict our analysis to flows for which the inertial effects can be ignored in the porous regions. This greatly simplifies the interface conditions and also allows us to neglect the convective terms $\langle \boldsymbol{v} \rangle \cdot \nabla \langle \boldsymbol{v} \rangle / \varepsilon$, $\nabla \cdot \langle \check{\boldsymbol{v}} \check{\boldsymbol{v}} \rangle$, and $\mu \boldsymbol{F} \cdot \langle \boldsymbol{v} \rangle / k$ in equation (2.3). This assumption is only valid for porous media of small permeability in which the flow velocities are small with respect to the characteristic velocity in the channel region. The convective effects become negligible because the dense structures of the porous matrix impede motion between layers of fluid. We thus limit our study to permeabilities for which the laminar interface velocity, $U(\pm h)$, is much smaller than the mean flow, U_m, in the channel, i.e. $U(\pm h) \ll U_m$. Following this assumption, the temporal term, $\rho(\partial \langle \boldsymbol{v} \rangle / \partial t)/\varepsilon$, in equation (2.3) is small compared to the Darcy term (see Whitaker 1996); however, we retain it because we expect the unsteady effects of the channel region to penetrate slightly into the porous regions.

The flow equations in the porous regions become

$$\frac{\rho}{\varepsilon_j} \frac{\partial \langle \boldsymbol{v}_j \rangle}{\partial t} = -\nabla \langle p_j \rangle^f + \frac{\mu}{\varepsilon_j} \nabla^2 \langle \boldsymbol{v}_j \rangle - \frac{\mu}{k_j} \langle \boldsymbol{v}_j \rangle, \quad j = 1, 2, \tag{2.5}$$

and

$$\nabla \cdot \langle \boldsymbol{v}_j \rangle = 0, \quad j = 1, 2, \tag{2.6}$$

and the momentum transfer conditions at the interfaces at $y = \pm h$ are

$$\boldsymbol{v} = \langle \boldsymbol{v}_j \rangle, \qquad p = \langle p_j \rangle^f, \quad j = 1, 2, \tag{2.7}$$

$$\frac{1}{\varepsilon_j} \frac{\partial \langle u_j \rangle}{\partial y} - \frac{\partial u}{\partial y} = \mp \frac{\tau_j}{\sqrt{k_j}} u, \qquad \frac{1}{\varepsilon_j} \frac{\partial \langle w_j \rangle}{\partial y} - \frac{\partial w}{\partial y} = \mp \frac{\tau_j}{\sqrt{k_j}} w, \quad j = 1, 2. \tag{2.8}$$

The subscript j refers to quantities in the lower, $j = 1$, and upper, $j = 2$, porous regions, respectively. Note from (2.7)–(2.8) that the velocity and pressure at an interface are continuous, while the shear stress has a jump proportional to the interface coefficient τ_j which accounts for the distribution of momentum at the interface. For a more thorough discussion of the physical significance of τ, we refer the reader to the work of Ochoa-Tapia & Whitaker (1995*a*, *b*). The coefficient τ depends on the manner in which a porous material's structure varies in the heterogeneous transition layer and on the surface machining of the interface. While there is recent work on determining τ theoretically (Goyeau *et al.* 2006; Chandesris & Jamet 2006), it must usually

be determined experimentally. Note that researchers often simply set $\tau = 0$, which generates an interface condition known as the Brinkman condition. Analytically, Ochoa-Tapia & Whitaker (1995*a*) found that the coefficient τ is of order one and may be either positive or negative. In a comparison with experiments by Beavers & Joseph (1967), Ochoa-Tapia & Whitaker (1995*b*) found that the coefficient τ varied roughly between -1.0 and 1.5 and can also be zero. When applying conditions (2.8) at the upper interface, a negative sign precedes τ_2 because the normal vector is defined as pointing into the channel region. In all subsequent equations, the symbol $\pm$ indicates that a positive sign is used when $j = 2$ and a negative sign is used when $j = 1$. The converse is true for the symbol $\mp$.

Note that a thorough literature review reveals several other competing methods of coupling a channel flow to an adjacent porous flow (see summary in Alazmi & Vafai 2001; Shavit *et al.* 2004). To the best of our knowledge, the methods of Beavers & Joseph (1967) and Ochoa-Tapia & Whitaker (1995*a*) show the best agreement with experiments. The method of Beavers & Joseph (1967) also uses an experimentally determined interface coefficient which accounts for the distribution of momentum at the interface. In this study, we use the approach of Ochoa-Tapia & Whitaker (1995*a*) because it is a more precise representation of the physics near the interface (see discussion in Ochoa-Tapia & Whitaker 1995*b*). Furthermore, while the approach of Beavers & Joseph (1967) produces a velocity discontinuity at an interface, the method of Ochoa-Tapia & Whitaker (1995*a*) produces a continuous profile that is closer to the true behaviour of the volume-averaged velocity in the transition region. This has been shown experimentally by Goharzadeh *et al.* (2005).

3. Laminar profile

A uniform longitudinal pressure gradient $\mathrm{d}p/\mathrm{d}x$ drives a fully developed laminar flow in both the channel and the porous layers. The flow in the channel region is governed by the following equation,

$$\frac{\mathrm{d}^2 u}{\mathrm{d}y^2} = \frac{1}{\mu}\frac{\mathrm{d}p}{\mathrm{d}x}, \tag{3.1}$$

while the flow in the porous regions is governed by the equation

$$\frac{k_j}{\varepsilon_j}\frac{\mathrm{d}^2\langle u_j\rangle}{\mathrm{d}y^2} - \langle u_j\rangle = \frac{k_j}{\mu}\frac{\mathrm{d}p}{\mathrm{d}x}, \quad j = 1, 2. \tag{3.2}$$

Because the pressure gradient is the same in all three regions, we have replaced $\mathrm{d}\langle p\rangle^f/\mathrm{d}x$ with $\mathrm{d}p/\mathrm{d}x$ in equation (3.2). Note that (3.2) is Darcy's equation with an added term, $k_j(\mathrm{d}^2\langle u_j\rangle/\mathrm{d}y^2)/\varepsilon_j$, called the Brinkman term. This term is only important in the Brinkman boundary layers near the interfaces where the laminar velocity decreases from its interface value to a constant value, $\langle u_j\rangle = k_j(\mathrm{d}p/\mathrm{d}x)/\mu$, called the Darcy velocity. Equations (3.1) and (3.2) are coupled at each interface, $y = \pm h$, by the momentum transfer conditions (2.7) and (2.8) and must also satisfy the no-slip condition, $\langle u_j\rangle = 0$, at the impermeable walls located at $y = \pm(h + 2h_j)$.

As discussed in § 2.2, at each interface there is a transition layer in which the structure of the porous medium undergoes rapid changes. Travelling within the transition layer, from the porous region towards the interface, the local porosity increases to unity (Ochoa-Tapia & Whitaker 1995*b*; Goharzadeh *et al.* 2005). Numerical and experimental studies of flows over packed beds of granular materials suggest that the Brinkman boundary layer thickness and the transition layer thickness

are both on the order of the particle diameter associated with this type of porous medium (see Sahraoui & Kaviany 1991; Ochoa-Tapia & Whitaker 1995*b*; Goharzadeh *et al.* 2005). Because the momentum transfer conditions of Ochoa-Tapia & Whitaker (1995*a*) assume that the porous regions are thicker than the transition layers, we restrict our analysis to porous regions that are at least twice as thick as the Brinkman layer, δ_B, associated with the interface. Using the definition suggested by Goharzadeh *et al.* (2005), we define δ_B as the distance, measured from an interface into the porous medium, at which the laminar velocity first approaches within 1 % of the Darcy velocity.

We found that the impermeable walls bounding the porous layers at $y = \pm(h+2h_j)$ have no influence on the laminar velocity in the channel region, the Brinkman layer, and the Darcy velocity, provided $h_j > \delta_B$. As we will see in § 4.3, we do not explicitly need the laminar velocity profile in the porous regions in order to solve the coupled linear stability problem. For simplicity, we therefore use the following non-dimensionalized laminar profile which assumes that the porous regions are semi-infinite. The laminar velocity profile in the channel region is

$$U = C\left[y^2 + \frac{B_1 - B_2}{A_1 - A_2}y + \frac{B_1A_2 - B_2A_1}{A_1 - A_2}\right], \tag{3.3}$$

while in the porous regions it is

$$\langle U_j\rangle = C\left\{\left[2\sigma_j^2 + 1 + \frac{\mp(B_2 - B_1) + B_1A_2 - B_2A_1}{A_1 - A_2}\right]\mathrm{e}^{(1\mp y)\sqrt{\varepsilon_j}/\sigma_j} - 2\sigma_j^2\right\}, \quad j = 1, 2, \tag{3.4}$$

where

$$C = \left[\frac{1}{3} + \frac{B_1A_2 - B_2A_1}{A_1 - A_2}\right]^{-1},$$

$$A_j = \mp 1 \mp \sigma_j\left[\frac{1}{\sqrt{\varepsilon_j}} - \tau_j\right]^{-1}, \quad j = 1, 2,$$

$$B_j = 2\sigma_j^2 + 1 + 2\sigma_j[1 + \tau_j\sigma_j]\left[\frac{1}{\sqrt{\varepsilon_j}} - \tau_j\right]^{-1}, \quad j = 1, 2,$$

and the symbol $\sigma_j = \sqrt{k_j}/h$ is the non-dimensional permeability in the porous regions. Equations (3.3) and (3.4) are general formulas valid for any σ_j, ε_j, and τ_j, within our assumptions, and have been non-dimensionalized using the channel half-height, h, as a characteristic length, and the ratio h/U_m, as a characteristic time, where U_m is the mean velocity in the channel region. Although the coordinate y in equations (3.3) and (3.4) is non-dimensional, for convenience we have kept the same notation as in the dimensional case. Note that Beavers & Joseph (1967) and Sparrow *et al.* (1973) defined the non-dimensional permeability as $\hat{\sigma}_j = 2h/\sqrt{k_j}$. We have chosen our definition in order to recover flow in a channel with impermeable walls as both σ_1 and σ_2 tend to zero. Beavers & Joseph (1967) interpret σ_j physically as a ratio between a length scale characterizing the permeable material, $\sqrt{k_j}$, and a length scale characterizing the channel region, h.

In our numerical calculations, we use the laminar velocity profile (3.3) and (3.4) which considers semi-infinitely wide porous layers, because at the small permeabilities, σ_j, considered in this study, it behaves better than the profile obtained for porous layers of finite height, given in Appendix A. The latter velocity profile contains sums

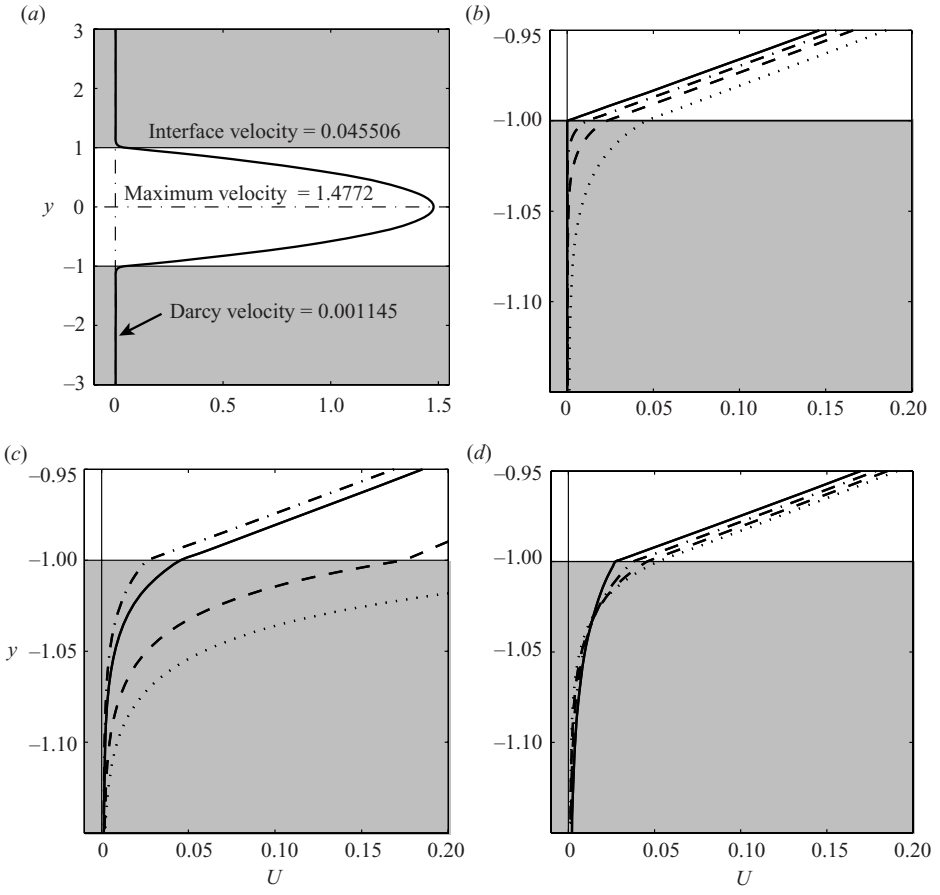

FIGURE 3. (*a*) The laminar velocity profile for the parameters $\sigma_1 = \sigma_2 = 0.02$, $\varepsilon_1 = \varepsilon_2 = 0.6$, $\tau_1 = \tau_2 = 0$, and $h_1 = h_2 = h$. (*b*) The laminar profile at the lower interface when the permeability is varied, $\sigma_1 = \sigma_2 =$ 0.0 (solid line), 0.005 (dash-dotted line), 0.01 (dashed line), and 0.02 (dotted line) ($\varepsilon_1 = \varepsilon_2 = 0.6$, $\tau_1 = \tau_2 = 0$, $h_1 = h_2 = h$). (*c*) The laminar profile at the lower interface when the interface coefficient is varied, $\tau_1 = \tau_2 = -1.0$ (dash-dotted line), 0.0 (solid line), 1.0 (dashed line), and 1.2 (dotted line) ($\sigma_1 = \sigma_2 = 0.02$, $\varepsilon_1 = \varepsilon_2 = 0.6$, $h_1 = h_2 = h$). (*d*) The laminar profile at the lower interface when the porosity is varied, $\varepsilon_1 = \varepsilon_2 = 0.2$ (solid line), 0.4 (dash-dotted line), 0.6 (dashed line), and 0.8 (dotted line) ($\sigma_1 = \sigma_2 = 0.02$, $\tau_1 = \tau_2 = 0$, $h_1 = h_2 = h$).

of terms of the form $\pm\exp(1/\sigma_j)$ which at small permeabilities become very large and cause significant rounding errors. The laminar velocity profile of a flow in a channel with only one porous wall is computed by setting either σ_1 or σ_2 in equations (3.3) and (3.4) to zero. The laminar velocity profile of a flow in a channel with two impermeable walls is recovered by setting both σ_1 and σ_2 in equations (3.3) and (3.4) to zero.

In order to investigate how σ_j, τ_j, and ε_j affect the laminar velocity profile, we vary σ_j while holding ε_j and τ_j constant, then we vary τ_j while holding σ_j and ε_j constant, and finally we vary ε_j while holding σ_j and τ_j constant. Figure 3(*a*) illustrates the laminar velocity profile generated using equations (3.3) and (3.4) and the parameters $\sigma_1 = \sigma_2 = 0.02$, $\varepsilon_1 = \varepsilon_2 = 0.6$, $\tau_1 = \tau_2 = 0$, and $h_1 = h_2 = h$. Note that the interface velocity is 4.55% U_m, one of the highest considered in our study, and the Darcy velocity outside the Brinkman layer is only on the order of 0.1% U_m. Figure 3(*b*)

illustrates the laminar velocity profile at the lower interface when the permeability is varied, $\sigma_1 = \sigma_2 = 0.0$, 0.005, 0.01, and 0.02, while holding $\varepsilon_1 = \varepsilon_2 = 0.6$, $\tau_1 = \tau_2 = 0$, and $h_1 = h_2 = h$ constant. Note that the laminar interface velocity and the Brinkman layer thickness, δ_B, both increase as the permeability increases. Also note that we recover flow in a channel with impermeable walls when $\sigma = 0.0$. Figure 3(*c*) illustrates the laminar velocity profile at the lower interface when the interface coefficient is varied, $\tau_1 = \tau_2 = -1.0$, 0.0, 1.0, and 1.2, while holding $\sigma_1 = \sigma_2 = 0.02$, $\varepsilon_1 = \varepsilon_2 = 0.6$, and $h_1 = h_2 = h$ constant. As τ increases, more momentum is transferred from the channel flow to the Brinkman layer, and both the laminar interface velocity and the Brinkman layer thickness increase. For this particular choice of parameters, τ above 1.2 begins to produce physically impossible laminar profiles with interface velocities that are larger than the maximum velocity in the channel region. Figure 3(*d*) illustrates the laminar profile at the lower interface when the porosity is varied, $\varepsilon_1 = \varepsilon_2 = 0.2$, 0.4, 0.6, and 0.8, while holding $\sigma_1 = \sigma_2 = 0.02$, $\tau_1 = \tau_2 = 0$, and $h_1 = h_2 = h$ constant. Note how the laminar interface velocity increases and the Brinkman layer thickness decreases with increasing ε.

4. Linear stability equations

4.1. *Non-dimensionalization of the governing equations*

We make the problem non-dimensional using the same characteristic length and time with which the laminar velocity profile (3.3) and (3.4) has been non-dimensionalized. We define the non-dimensional pressure as $p/\rho U_m^2$, and the Reynolds number as $Re = \rho U_m h/\mu$. We use capital italics to represent the non-dimensionalized velocity, $\langle U_1 \rangle$, U, and $\langle U_2 \rangle$, and pressure, $P(x)$, of the fully developed laminar flow, or base flow. All subsequent equations are non-dimensional except when explicitly noted.

The non-dimensionalized channel flow equations are

$$\frac{\partial \boldsymbol{v}}{\partial t} + \boldsymbol{v} \cdot \nabla \boldsymbol{v} = -\nabla p + \frac{1}{Re} \nabla^2 \boldsymbol{v}, \tag{4.1}$$

and

$$\nabla \cdot \boldsymbol{v} = 0, \tag{4.2}$$

while the non-dimensionalized porous flow equations become

$$\frac{1}{\varepsilon_j} \frac{\partial \langle \boldsymbol{v}_j \rangle}{\partial t} = -\nabla \langle p_j \rangle^f + \frac{\nabla^2 \langle \boldsymbol{v}_j \rangle}{\varepsilon_j Re} - \frac{\langle \boldsymbol{v}_j \rangle}{\sigma_j^2 Re}, \quad j = 1, 2, \tag{4.3}$$

and

$$\nabla \cdot \langle \boldsymbol{v}_j \rangle = 0, \quad j = 1, 2. \tag{4.4}$$

The non-dimensionalized momentum transfer conditions at the interfaces at $y = \pm 1$ become

$$\boldsymbol{v} = \langle \boldsymbol{v}_j \rangle, \qquad p = \langle p_j \rangle^f, \quad j = 1, 2, \tag{4.5}$$

$$\frac{\sigma_j}{\varepsilon_j} \frac{\partial \langle u_j \rangle}{\partial y} - \sigma_j \frac{\partial u}{\partial y} = \mp \tau_j u, \qquad \frac{\sigma_j}{\varepsilon_j} \frac{\partial \langle w_j \rangle}{\partial y} - \sigma_j \frac{\partial w}{\partial y} = \mp \tau_j w, \quad j = 1, 2, \tag{4.6}$$

and the boundary conditions at $y = \pm (1 + 2h_j/h)$ are

$$\langle \boldsymbol{v}_j \rangle = 0, \quad j = 1, 2. \tag{4.7}$$

4.2. *Linear stability equations in the channel region*

We analyse the stability of the fully developed laminar flow, or base flow, in the channel region, $U(y)$ and $P(x)$, with respect to small planar wave perturbations, $\hat{\boldsymbol{v}} = [\hat{u}\ \hat{v}\ \hat{w}]^T$ and $\hat{p}$, of the form

$$\begin{pmatrix} \hat{\boldsymbol{v}} \\ \hat{p} \end{pmatrix} = \begin{pmatrix} \widetilde{\boldsymbol{v}}(y) \\ \widetilde{p}(y) \end{pmatrix} \mathrm{e}^{\mathrm{i}(\alpha x + \beta z - \alpha c t)}, \tag{4.8}$$

where $|\hat{\boldsymbol{v}}/U| \ll 1$ and $|\hat{p}/P| \ll 1$. The perturbations $\hat{\boldsymbol{v}}$ and $\hat{p}$ travel in the direction $(\alpha, 0, \beta)$ with streamwise and spanwise wavenumbers α and β, respectively, and a wall-normal structure given by the amplitude functions $\widetilde{\boldsymbol{v}}(y)$ and $\widetilde{p}(y)$. We consider a temporal linear stability analysis where the wavenumbers, α and β, are assumed to be real, while the streamwise phase speed, $c = c_r + \mathrm{i}c_i$, and the amplitude functions are in general complex. A perturbation is unstable when the imaginary part of the phase speed is positive, $c_i > 0$.

The linear stability equations for the channel region are obtained by substituting the perturbed base flow, $U(y) + \hat{\boldsymbol{v}}$ and $P(x) + \hat{p}$, into equations (4.1) and (4.2) and linearizing them. Equation (4.8) is then used to obtain the well-known Orr–Sommerfeld equation

$$\left[(U - c)(\mathrm{D}^2 - \kappa^2) - U'' - \frac{1}{\mathrm{i}\alpha Re}(\mathrm{D}^2 - \kappa^2)^2\right] \widetilde{v}(y) = 0, \tag{4.9}$$

and Squire equation

$$\left[(U - c) - \frac{1}{\mathrm{i}\alpha Re}(\mathrm{D}^2 - \kappa^2)\right] \widetilde{\eta}(y) = -\frac{\beta U' \widetilde{v}}{\alpha}, \tag{4.10}$$

where a prime and D both denote $\mathrm{d}/\mathrm{d}y$, $\kappa = \sqrt{\alpha^2 + \beta^2}$, $\widetilde{v}$ is the amplitude of the wall-normal velocity perturbation, and $\widetilde{\eta} = \partial\widetilde{u}/\partial z - \partial\widetilde{w}/\partial x$ is the amplitude of the wall-normal vorticity perturbation, respectively. We refer the reader to Schmid & Henningson (2001) for a more thorough derivation of equations (4.9) and (4.10).

4.3. *Linear stability equations in the porous regions*

Because the porous flow equations (4.3) and (4.4) are linear, there is no need to linearize them about the laminar base flow, $\langle U_j \rangle$. We assume that the perturbations in the porous regions also have wave-like forms given by

$$\begin{pmatrix} \langle \hat{\boldsymbol{v}}_j \rangle \\ \langle \hat{p}_j \rangle^f \end{pmatrix} = \begin{pmatrix} \widetilde{\boldsymbol{v}}_j(y) \\ \widetilde{p}_j(y) \end{pmatrix} \mathrm{e}^{\mathrm{i}(\alpha x + \beta z - \alpha c t)}, \quad j = 1, 2, \tag{4.11}$$

so that the wave-like perturbations in all three regions have identical wavenumbers and phase speeds. The linear stability equations for the porous regions are obtained by substituting expressions (4.11) into equations (4.3) and (4.4) and rearranging the resulting equations for $\widetilde{\boldsymbol{v}}_j(y)$ and $\widetilde{p}_j$ into the following counterparts to the Orr–Sommerfeld and Squire equations in the porous regions:

$$\left[-c(\mathrm{D}^2 - \kappa^2) - \frac{1}{\mathrm{i}\alpha Re}(\mathrm{D}^2 - \kappa^2)^2 + \frac{\varepsilon_j}{\mathrm{i}\alpha\sigma_j^2 Re}(\mathrm{D}^2 - \kappa^2)\right] \widetilde{v}_j(y) = 0, \quad j = 1, 2, \tag{4.12}$$

and

$$\left[-c - \frac{1}{\mathrm{i}\alpha Re}(\mathrm{D}^2 - \kappa^2) + \frac{\varepsilon_j}{\mathrm{i}\alpha\sigma_j^2 Re}\right]\widetilde{\eta}_j(y) = 0, \quad j = 1, 2. \tag{4.13}$$

Note that because inertial effects have been neglected in the porous regions, equations (4.12) and (4.13) lack any term directly coupling the disturbances in the porous regions with the laminar profile in the porous regions. For the same reason, equation (4.13) is homogeneous, unlike the Squire equation (4.10). However, the stability equations (4.12) and (4.13) have new terms, $\varepsilon_j(\mathrm{D}^2 - \kappa^2)/\mathrm{i}\alpha\sigma_j^2 Re$ and $\varepsilon_j/\mathrm{i}\alpha\sigma_j^2 Re$, respectively, arising from the Darcy drag term.

Squire's transformation states that for each unstable three-dimensional disturbance, $\widetilde{v}$, there is a corresponding unstable two-dimensional disturbance at a smaller Reynolds number. To show that Squire's transformation holds in both the channel and the porous regions, consider that a three-dimensional disturbance obeys equations (4.9) and (4.12), while a two-dimensional disturbance obeys the equations below, found by setting $\beta = 0$, $\alpha = \hat{\alpha}$, and $Re = \widehat{Re}$:

$$\left[(U - c)(\mathrm{D}^2 - \hat{\alpha}^2) - U'' - \frac{1}{\mathrm{i}\hat{\alpha}\widehat{Re}}(\mathrm{D}^2 - \hat{\alpha}^2)^2\right]\widetilde{v}(y) = 0, \tag{4.14}$$

and

$$\left[c(\mathrm{D}^2 - \hat{\alpha}^2) + \frac{1}{\mathrm{i}\hat{\alpha}\widehat{Re}}(\mathrm{D}^2 - \hat{\alpha}^2)^2 - \frac{\varepsilon_j}{\mathrm{i}\sigma_j^2\hat{\alpha}\widehat{Re}}(\mathrm{D}^2 - \hat{\alpha}^2)\right]\widetilde{v}_j = 0, \quad j = 1, 2. \tag{4.15}$$

Equations (4.9) and (4.12) have identical solutions to (4.14) and (4.15) as long as $\hat{\alpha} = \kappa$ and $\hat{\alpha}\widehat{Re} = \alpha Re$. Hence,

$$\widehat{Re} = \frac{\alpha}{\kappa} Re < Re.$$

Thus, for each unstable three-dimensional disturbance with the Reynolds number, Re, there is a corresponding unstable two-dimensional disturbance with a smaller Reynolds number, $\widehat{Re}$.

4.4. *Boundary and interface conditions*

Using the momentum transfer conditions (4.5)–(4.6), we derive the conditions coupling $\widetilde{v}$ and $\widetilde{v}_j$ at the interfaces located at $y = \pm 1$:

$$\widetilde{v} = \widetilde{v}_j, \qquad \frac{\mathrm{d}\widetilde{v}}{\mathrm{d}y} = \frac{\mathrm{d}\widetilde{v}_j}{\mathrm{d}y}, \quad j = 1, 2, \tag{4.16}$$

$$-\frac{\sigma_j}{\varepsilon_j}\frac{\mathrm{d}^2\widetilde{v}_j}{\mathrm{d}y^2} + \sigma_j\frac{\mathrm{d}^2\widetilde{v}}{\mathrm{d}y^2} = \pm\tau_j\frac{\mathrm{d}\widetilde{v}}{\mathrm{d}y}, \quad j = 1, 2, \tag{4.17}$$

$$\left[\left(\frac{1}{\varepsilon_j} - 1\right)\left(\mathrm{i}\alpha c - \frac{\kappa^2}{Re}\right) - \frac{1}{\sigma_j^2 Re} + \mathrm{i}\alpha U\right]\frac{\mathrm{d}\widetilde{v}}{\mathrm{d}y} + \frac{1}{Re}\frac{\mathrm{d}^3}{\mathrm{d}y^3}\left(\frac{\widetilde{v}_j}{\varepsilon_j} - \widetilde{v}\right) - \mathrm{i}\alpha U'_{ch}\widetilde{v} = 0, \quad j = 1, 2, \tag{4.18}$$

and the conditions coupling $\widetilde{\eta}$ and $\widetilde{\eta}_j$ at each interface

$$\widetilde{\eta} = \widetilde{\eta}_j, \qquad \frac{\sigma_j}{\varepsilon_j}\frac{\mathrm{d}\widetilde{\eta}_j}{\mathrm{d}y} - \sigma_j\frac{\mathrm{d}\widetilde{\eta}}{\mathrm{d}y} = \mp\tau_j\widetilde{\eta}, \quad j = 1, 2, \tag{4.19}$$

where U'_{ch} denotes the value of U' evaluated on the channel side of the interface because U' is generally discontinuous at the interface. The perturbations must also satisfy the boundary conditions at the impermeable walls located at $y = \pm(1+2h_j/h)$,

$$\widetilde{\eta}_j = \widetilde{v}_j = \frac{\mathrm{d}\widetilde{v}_j}{\mathrm{d}y} = 0, \quad j = 1, 2. \tag{4.20}$$

5. Solution of the coupled linear stability problem

In this section, we illustrate the numerical method we use to solve the fully coupled linear stability problem. For simplicity, we discuss the case where $h_1 = h_2 = h$. The problem in the channel region is solved with respect to the axes (x, y, z) with origin located on the channel centreline, while the problems in the porous regions 1 and 2 are solved with respect to coordinate systems (x_1, y_1, z_1) and (x_2, y_2, z_2), respectively, with origins located midway between the interfaces and the impermeable walls.

We approximate the perturbation amplitude functions $\widetilde{v}(y)$, $\widetilde{v}_1(y_1)$, and $\widetilde{v}_2(y_2)$ using three finite Chebyshev expansions,

$$\widetilde{v}(y) = \sum_{n=0}^{N} a_n T_n(y), \tag{5.1}$$

$$\widetilde{v}_1(y_1) = \sum_{n=0}^{N} d_n T_n(y_1), \qquad \widetilde{v}_2(y_2) = \sum_{n=0}^{N} e_n T_n(y_2). \tag{5.2}$$

In the channel region, we force expansion (5.1) to satisfy the Orr–Sommerfeld equation (4.9) at the Gauss–Lobatto points, $y_n = \cos(n\pi/N)$, where $n = 0, \ldots, N$ (e.g. Schmid & Henningson 2001). This produces the generalized eigenvalue problem

$$\boldsymbol{A}\boldsymbol{a} = c\boldsymbol{B}\boldsymbol{a}, \tag{5.3}$$

for the eigenvalue c and eigenvector $\boldsymbol{a}$ of the $N+1$ expansion coefficients a_n. Similarly, in the porous regions 1 and 2, we force expansions (5.2) to satisfy equation (4.12) at the Gauss–Lobatto points on the wall-normal axes y_1 and y_2, respectively. This produces two more generalized eigenvalue problems,

$$\boldsymbol{D}\boldsymbol{d} = c\sigma_1^2\boldsymbol{B}\boldsymbol{d}, \qquad \boldsymbol{E}\boldsymbol{e} = c\sigma_2^2\boldsymbol{B}\boldsymbol{e}, \tag{5.4}$$

for the eigenvalue c and the eigenvectors $\boldsymbol{d}$ and $\boldsymbol{e}$ of the $N+1$ expansion coefficients d_n and e_n, respectively.

To solve the coupled eigenvalue problem, we assemble the three matrix equations (5.3)–(5.4) in the following compound matrix equation

$$\begin{pmatrix} \boldsymbol{E} & 0 & 0 \\ 0 & \boldsymbol{A} & 0 \\ 0 & 0 & \boldsymbol{D} \end{pmatrix} \begin{pmatrix} \boldsymbol{e} \\ \boldsymbol{a} \\ \boldsymbol{d} \end{pmatrix} = c \begin{pmatrix} \sigma_2^2\boldsymbol{B} & 0 & 0 \\ 0 & \boldsymbol{B} & 0 \\ 0 & 0 & \sigma_1^2\boldsymbol{B} \end{pmatrix} \begin{pmatrix} \boldsymbol{e} \\ \boldsymbol{a} \\ \boldsymbol{d} \end{pmatrix}, \tag{5.5}$$

and impose the boundary and interface conditions following the procedure outlined by Schmid & Henningson (2001): the expansions (5.1)–(5.2) are substituted into the conditions (4.16)–(4.18) and (4.20), and the resulting twelve conditions are imposed by replacing 12 rows of the compound matrix equation (5.5).

To determine the number N of Chebyshev polynomials necessary to accurately resolve the problem, we verify convergence with respect to the twenty least stable

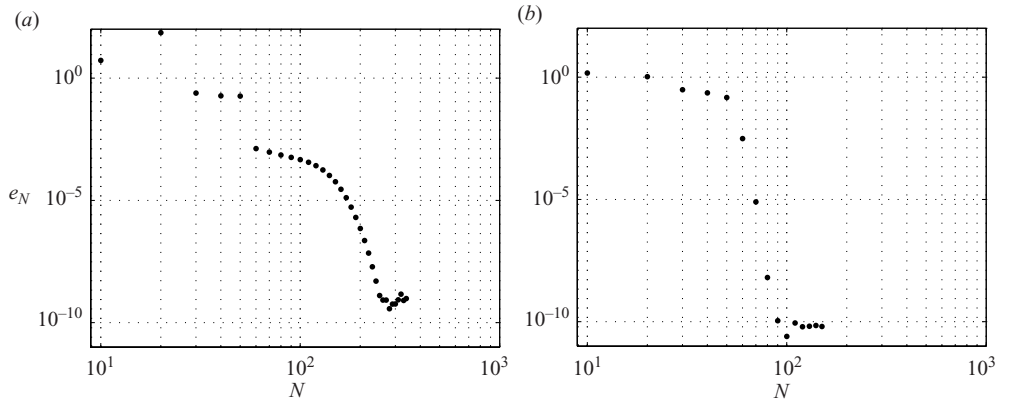

FIGURE 4. Log-log plots of the relative error, e_N, versus the number of Chebyshev polynomials used to solve the problem, N. The parameters are $\varepsilon_1 = \varepsilon_2 = 0.6$, $\tau_1 = \tau_2 = 0.5$, $h_1 = h_2 = h$, $Re = 2000$, $\alpha = 1$, $\beta = 1$, (*a*) $\sigma_1 = \sigma_2 = 0.0005$, (*b*) $\sigma_1 = \sigma_2 = 0.01$.

eigenvalues. Using the L^2 norm, we define the relative error for a given N as

$$e_N = \frac{\|\boldsymbol{c}_{N+1} - \boldsymbol{c}_N\|_2}{\|\boldsymbol{c}_N\|_2},$$

where $\boldsymbol{c}_N$ and $\boldsymbol{c}_{N+1}$ are vectors whose components are the twenty least stable eigenvalues generated using N and $N+1$ Chebyshev polynomials, respectively, in each region. Small permeabilities require many collocation points near the interfaces in order to resolve the behaviour of the disturbances in the small Brinkman layers. As a result, the number of polynomials required for convergence generally tends to increase as the permeability decreases. For permeabilities on the order of $\sigma = 0.01$, roughly 100 polynomials are sufficient in each region to attain an error on the order of 10^{-10}: see figure 4(*b*). Very small permeabilities below $\sigma = 0.0005$, however, can require up to 300 polynomials in each region to attain an error on the order of 10^{-9}: see figure 4(*a*). The number of polynomials required for convergence also tends to increase as the half-heights of the porous regions, h_j, $j = 1, 2$, increase, because this stretches the Gauss–Lobatto points over a greater interval. For each particular choice of permeabilities and half-heights of the porous layers, we always attempt to use the minimum N for which the corresponding error plot reaches the minimum-possible error, which is usually on the order of 10^{-9} or 10^{-10}, as illustrated in figure 4.

6. Linear stability results for symmetric laminar velocity profiles

Wall permeability affects the linear stability of a channel flow by altering the laminar velocity profile and allowing the presence of non-zero perturbation velocities at the porous interfaces. Beavers & Joseph (1967) observed that the velocity profile of a fully developed laminar flow in a channel with porous walls is skewed toward the wall with larger interface velocity. Fu & Joseph (1970) found that asymmetric laminar velocity profiles in channels with impermeable walls tend to be linearly more stable than symmetric velocity profiles provided the asymmetric profiles have no inflection points. In order to investigate the effects of the normal and tangential velocity components at the porous interfaces and remove the stabilizing effect of a skewed laminar velocity profile, we begin our study by considering the linear stability of symmetric laminar velocity profiles in channels with two identical porous walls.

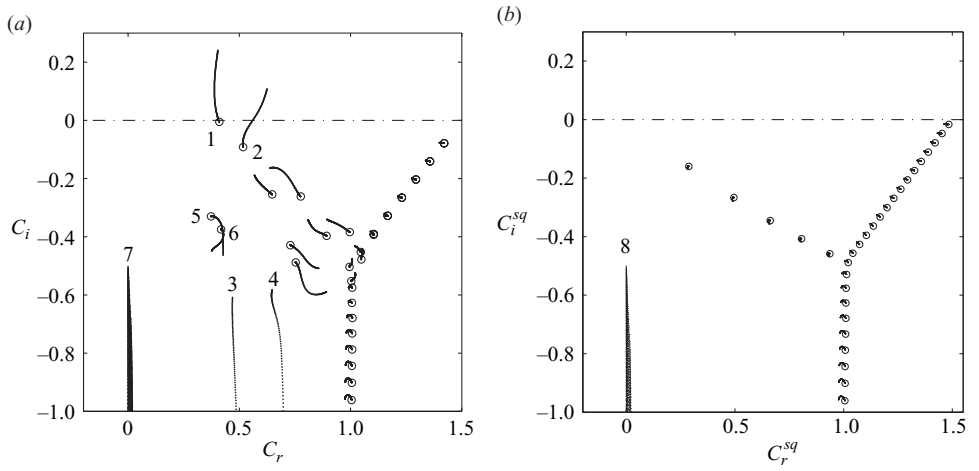

FIGURE 5. Using the constant parameters $\varepsilon = 0.6$, $\tau = 0$, and $h_p = h$: (*a*) the trajectory of the Orr–Sommerfeld eigenvalues for $Re = 3000$, $\alpha = 1$, and $\beta = 0$ as σ is increased from $\sigma_{min} = 0.0002$ (circled) to $\sigma_{max} = 0.02$; (*b*) the trajectory of the Squire spectrum for $Re = 3000$, $\alpha = 1$, and $\beta = 1$ as σ is increased from $\sigma_{min} = 0.0002$ (circled) to $\sigma_{max} = 0.02$.

The stability of skewed laminar velocity profiles will be considered separately in § 7. For simplicity, in this section we will drop the subscript $j = 1, 2$ denoting the upper and lower porous regions and use simply σ, ε, τ, and h_p to denote the permeability, porosity, interface coefficient, and half-height, respectively, of the two identical porous layers.

This section significantly extends the work of Tilton & Cortelezzi (2006) and is organized in the following manner. In § 6.1, we investigate the effects of permeability, σ, on the linear stability of a symmetric laminar velocity profile in a channel characterized by the parameters $\varepsilon = 0.6$, $\tau = 0$, $h_p = h$, and $0.0002 < \sigma < 0.02$ in great detail. In § 6.2, we investigate the effects of the interfacial coefficient, τ, by varying τ between -1 and 1. In § 6.3, we investigate the effects of the height of the porous regions, h_p, by varying h_p between $0.25h$ and $2h$. In § 6.4, we discuss the validity of ignoring inertial effects in the porous regions, and in § 6.5, we fit the parameters ε and τ so that the porous materials we model behave like foametal and aloxite, two materials used in the experiments of Beavers & Joseph (1967).

6.1. *The effects of permeability, σ, on linear stability*

To characterize the effects of permeability, we fix the parameters $\varepsilon = 0.6$, $\tau = 0$, and $h_p = h$, and vary only the non-dimensional permeability, $\sigma = \sqrt{k}/h$, below a maximum value consistent with our requirement that the laminar interface velocity, $U(\pm 1)$, is much less than the mean laminar velocity, U_m, in the channel region. This procedure is equivalent to laboratory experiments which vary the non-dimensional permeability by varying the channel half-height h (Beavers & Joseph 1967; Beavers *et al.* 1970; Sparrow *et al.* 1973), since when h increases, $\sigma = \sqrt{k}/h$ decreases and vice versa. Note that there is no way to choose the maximum-allowable interface velocity without first obtaining an estimate for the critical Reynolds number. We therefore begin by setting the maximum-allowable interface velocity, $U(\pm 1)$, to a reasonable value of 5 % U_m. In § 6.4, we use our results for the critical Reynolds numbers to verify this choice.

Figure 5(*a*) illustrates the trajectory of the Orr–Sommerfeld eigenvalues as the permeability is increased from $\sigma_{min} = 0.0002$ to $\sigma_{max} = 0.02$, for $Re = 3000$, $\alpha = 1$, and

$\beta = 0$. The maximum permeability corresponds to a maximum laminar interface velocity of 4.55 % U_m. The laminar velocity profile for σ_{max} is illustrated in figure 3(*a*). The circled eigenvalues in figure 5(*a*) correspond to σ_{min} and are within 3 decimal places of the eigenvalues associated with a corresponding channel flow with impermeable walls. Note that the circled eigenvalues in figure 5(*a*) are located on three branches. The eigenvalues on the upper left branch are called wall modes because their eigenfunctions, $\tilde{v}$, vary mostly near the wall. For this reason, we expect that permeability will affect these modes more than the others. The eigenvalues on the upper right branch are called centre modes because their eigenfunctions, $\tilde{v}$, vary mostly near the centre of the channel. The modes on the lower branch are highly damped.

Permeability destabilizes two Orr–Sommerfeld wall modes, labelled 1 and 2 in figure 5(*a*). Wall mode 1 becomes unstable at a critical permeability of $\sigma_c = 0.00222$ for which the laminar interface velocity is only 0.515 % U_m. Wall mode 2 becomes unstable at a critical permeability of $\sigma_c = 0.01264$ for which the laminar interface velocity is 2.899 % U_m. At σ_{max}, wall modes 1 and 2 have exponential growth rates, αc_i, of 0.2404 and 0.1081, respectively. Figure 6(*a*) illustrates the eigenfunction, $\tilde{v}$, of wall mode 1 at σ_{min}. The amplitude of the perturbation velocity vanishes at the interfaces, and we recover the Tollmien–Schlichting wave observed in a channel flow with impermeable walls. Figure 6(*b*) illustrates the same eigenfunction at $\sigma_{max} = 0.02$. The amplitude of the perturbation velocity no longer vanishes at the interfaces and decreases monotonically in the porous regions.

Permeability introduces two new wall modes, labelled 3 and 4 in figure 5(*a*), which are similar in structure to the pre-existing wall modes labelled 5 and 6 respectively. Note that the trajectories of modes 5 and 6 in figure 5(*a*) intersect and may be hard to distinguish visually. It may help the reader to know that at $\sigma_{max} = 0.02$, mode 5 is to the right of mode 6. The eigenfunctions corresponding to modes 3, 4, 5 and 6 are illustrated in figures 6(*c*)–6(*f*) for $\sigma_{max} = 0.02$. Note that the eigenfunctions of modes 3 and 5 are symmetric, while the eigenfunctions of modes 4 and 6 are antisymmetric, and that the eigenfunctions of modes 3 and 4 have one more oscillation near the interfaces than modes 5 and 6.

Permeability introduces a group of new eigenvalues labelled 7 in figure 5(*a*). These eigenvalues occur in repeated pairs and approach the real axis, but never become unstable, as the permeability increases. We refer to them as *porous modes* because their eigenfunctions vary mostly in the porous regions. For each of these pairs of repeated eigenvalues there is a corresponding pair of eigenfunctions, one of which is symmetric and the other of which is antisymmetric, as illustrated in figures 6(*g*) and 6(*h*). Note that these modes have small, but non-zero, phase speeds, c_r. The least stable pair, for example, has a phase speed of 0.000155 at σ_{max}. The ensemble of these modes appears to indicate the existence of a continuous spectrum as the thickness of the porous layers tends to infinity. When solving the Orr–Sommerfeld equation for an infinite or semi-infinite domain, one generally encounters a discrete spectrum and a continuous spectrum. The Blasius boundary layer, for example, has a discrete spectrum and a continuous spectrum that is a vertical line in the complex plane (e.g. see Schmid & Henningson 2001). Sparrow *et al.* (1973) also noted the analogy between the spectral features of the current problem and those of the Blasius boundary layer. The analogy is due to the fact that in a Blasius boundary layer flow, the perturbation velocity diminishes in the free stream, while in the current problem, the perturbation velocity diminishes in the porous regions.

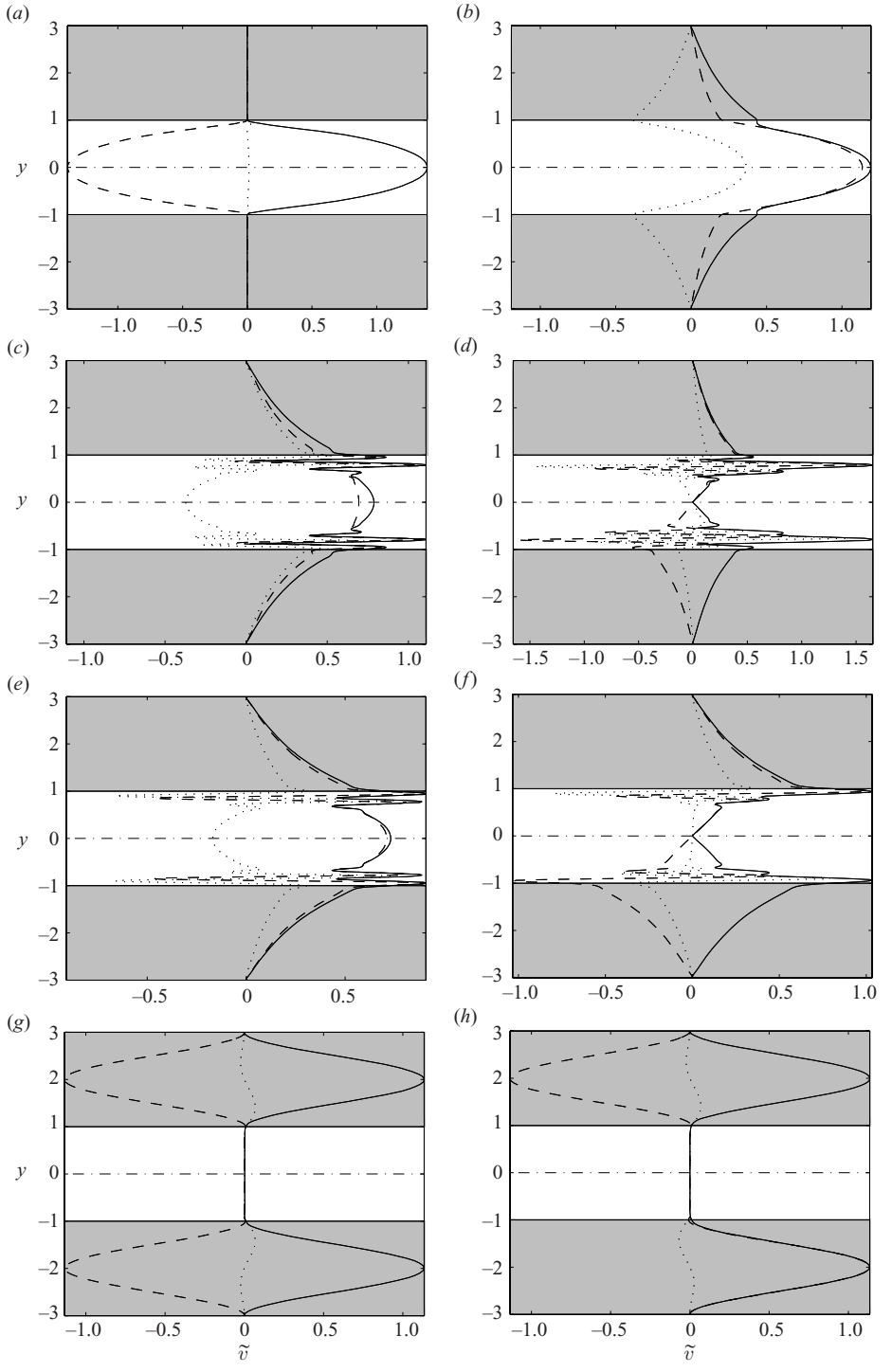

FIGURE 6. Eigenfunctions, $|\widetilde{v}|$ (solid line), $\widetilde{v}_r$ (dashed line), $\widetilde{v}_i$ (dotted line), of selected eigenvalues labelled in figure 5(*a*): (*a*) mode 1 at σ_{min}; (*b*) mode 1 at σ_{max}; (*c*) mode 3 at σ_{max}; (*d*) mode 4 at σ_{max}; (*e*) mode 5 at σ_{max}; (*f*) mode 6 at σ_{max}; (*g*) and (*h*) least stable pair of porous modes at σ_{max}.

	αc_i			
Re	$\sigma = 0.0$	$\sigma = 0.0002$	$\sigma = 0.002$	$\sigma = 0.02$
2000	−0.015277	−0.015239	−0.012495	0.191007
3000	−0.004750	−0.004708	−0.000907	0.240428
4000	0.000485	0.000532	0.005388	0.269851
5000	0.003354	0.003407	0.009311	0.289311

TABLE 1. For the Reynolds numbers in the left column, the columns to the right show the growth rate, αc_i, of the eigenvalue labelled 1 in figure 5(*a*) when the permeability is $\sigma = 0.0$ (second column), $\sigma = 0.0002$ (third column), 0.002 (fourth column), and 0.02 (fifth column). All other parameters are held constant: $\alpha = 1$, $\beta = 0$, $\varepsilon = 0.6$, $\tau = 0$, and $h_p = h$.

Table 1 shows the numerical values for the growth rate, αc_i, of the Tollmien–Schlichting wave, which is labelled 1 in figure 5(*a*), when the Reynolds number is $Re = 2000$, 3000, 4000, and 5000, and the permeability is $\sigma = 0.0$, 0.0002, 0.002, and 0.02. All other parameters are held constant: $\alpha = 1$, $\beta = 0$, $\varepsilon = 0.6$, $\tau = 0$, and $h_p = h$. Note that the growth rates for the minimum permeability, $\sigma_{min} = 0.0002$, are within three decimal places of those for $\sigma = 0.0$. As the permeability increases to $\sigma = 0.002$ and 0.02, however, the growth rates are considerably larger than those for $\sigma = 0.0$. Also note how the increase in growth rate due to an increase in Reynolds number increases with permeability and is greater in a channel with porous walls than in a channel with impermeable walls. Similar behaviour has been observed with the eigenvalues labelled 2, 3, 4, and 7, in figure 5(*a*).

When $\tilde{v} = 0$, the Orr–Sommerfeld equation (4.9) is identically zero and the Squire equation (4.10) is homogeneous and constitutes an eigenvalue problem for a new set of eigenvalues, $c^{sq} = c_r^{sq} + \mathrm{i}c_i^{sq}$, called Squire modes. We have added the superscript to stress that the Squire modes, c^{sq}, are generally different from the Orr–Sommerfeld modes, c. Figure 5(*b*) illustrates the trajectory of the Squire eigenvalues for $Re = 3000$, $\alpha = 1$, and $\beta = 1$ as the permeability, σ, is increased from $\sigma_{min} = 0.0002$ to $\sigma_{max} = 0.02$. The circled eigenvalues correspond to σ_{min} and are within 3 decimal places of the eigenvalues associated with a corresponding flow in a channel with impermeable walls. Permeability again introduces a new class of porous modes, labelled 8 in figure 5(*b*), but does not significantly affect the pre-existing modes. In all the cases we have considered, we have observed that wall permeability does not destabilize the Squire modes. We thus set the spanwise wavenumber, β, to zero when computing the neutral curves.

Figure 7(*a*) illustrates the effects of permeability on the neutral curve. The neutral curve for a channel flow with impermeable walls ($\sigma = 0.0$) is illustrated to the right, with the unstable region shaded a dark grey. The neutral curves for $\sigma = 0.002$, 0.006, and 0.02 are represented with solid lines and the corresponding unstable regions are shaded with successively lighter shades of grey. Note how the shaded unstable regions become larger and more blunt as permeability increases. As a result, the number of unstable wavenumbers, α, for a fixed Reynolds number, increases as the permeability increases.

Figure 7(*b*) illustrates the dependence of the critical Reynolds number on the permeability. The critical Reynolds number at $\sigma_{min} = 0.0002$ is 3835.49, while the corresponding Poiseuille value is 3848.17. As the permeability increases, the critical Reynolds number drops sharply and eventually reaches a value of 416.03 at σ_{max},

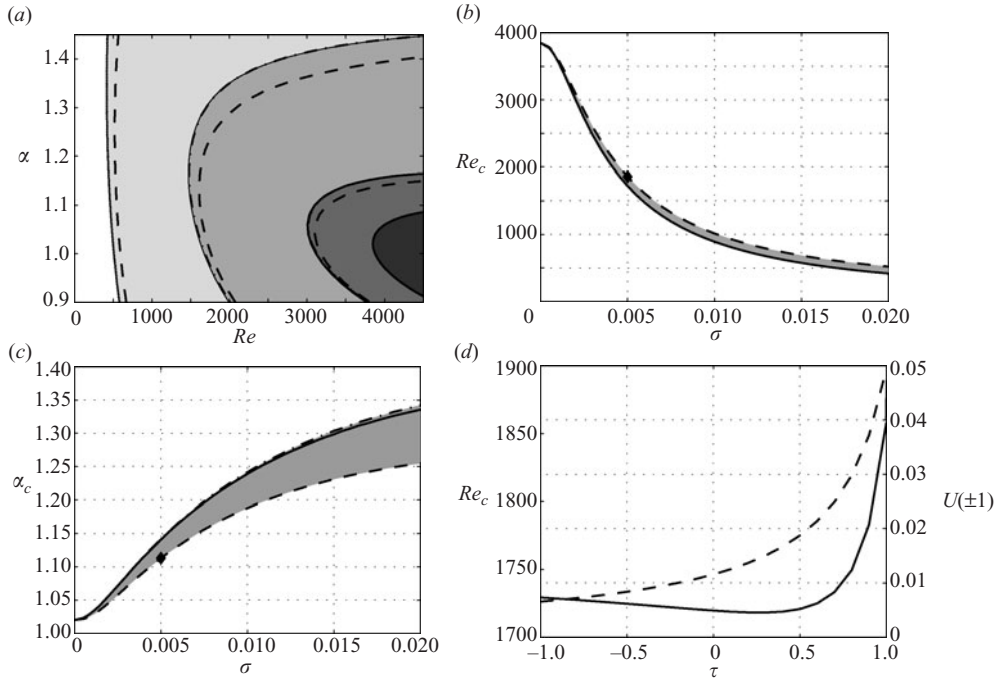

FIGURE 7. (*a*) The neutral curves for $\sigma = 0.0$, 0.002, 0.006, and 0.02 using $\varepsilon = 0.6$, $h_p = h$, and $\tau = -1.0$ (dash-dotted lines), 0.0 (solid lines) and 1.0 (dashed lines). The unstable regions for $\sigma = 0.0$ (darkest grey), 0.002, 0.006, 0.02 (lightest grey) using $\varepsilon = 0.6$, $h_p = h$, and $\tau = 0$ are shaded progressively lighter shades of grey. (*b*) The critical Reynolds number, Re_c, vs permeability, σ, using $\varepsilon = 0.6$, $h_p = h$, and $\tau = -1.0$ (dash-dotted line), 0.0 (solid line), and 1.0 (dashed line). (*c*) The critical wavenumber, α_c, vs. permeability, σ, using $\varepsilon = 0.6$, $h_p = h$, and $\tau = -1.0$ (dash-dotted line), 0.0 (solid line), and 1.0 (dashed line). (*d*) The laminar interface velocity, $U(\pm 1)$ (dashed line), and the critical Reynolds number, Re_c (solid line), vs τ, using $\sigma = 0.005$, $\varepsilon = 0.6$, and $h_p = h$.

or roughly 10 % of the corresponding Poiseuille value. Meanwhile, the critical wavenumber, illustrated in figure 7(*c*), increases from a value of 1.02 at σ_{min}, which is equal to the corresponding value for a channel flow with impermeable walls, to 1.34 at σ_{max}.

6.2. *The effects of varying τ on linear stability*

To characterize the effects of the interfacial coefficient, τ, we have repeated the analysis presented in § 6.1 for $\tau = 1$ and -1. Figure 7(*a*) illustrates that the neutral curves for $\tau = -1$ (dash-dotted line) are nearly indistinguishable from those for $\tau = 0$ (solid line), while those for $\tau = 1$ (dashed line) are significantly more stable. Figure 7(*b*) illustrates the dependence of the critical Reynolds number on the permeability for $\tau = -1$, 0, and 1. The results for $\tau = -1$ (dash-dotted line) are again nearly indistinguishable from the results for $\tau = 0$ (solid line), while the results for $\tau = 1$ (dashed line) are noticeably more stable. At σ_{max}, the critical Reynolds number for $\tau = -1$ (dash-dotted line) is 416.524, roughly 0.1 % greater than the result for $\tau = 0$ (solid line), while the critical Reynolds number for $\tau = 1$ (dashed line) is 519.459, roughly 25 % greater than the result for $\tau = 0$ (solid line). Figure 7(*c*) illustrates that the critical wavenumbers for $\tau = -1$ (dash-dotted line) are nearly indistinguishable from those for $\tau = 0$ (solid line) except near σ_{max}, while the critical wavenumbers for $\tau = 1$ (dashed line) are significantly smaller. The regions between the upper and lower curves in figures 7(*b*)–7(*c*)

have been shaded to represent the sort of error one may incur by assuming the Brinkman condition, $\tau = 0$, in cases when $\tau \neq 0$.

Note that the laminar interface velocity for a given permeability increases with τ. We have marked the curves for $\tau = 1$ in figures 7(*b*) and 7(*c*) with a diamond at the permeability, $\sigma = 0.005$, at which the laminar interface velocity is close to 5 % U_m. The diamond indicates that higher permeabilities may violate the maximum-allowable laminar interface velocity and inertial effects may, as a result, be non-negligible in the porous regions. The increase in the tangential interface velocity with τ is one possible explanation for the increase in critical Reynolds number between $\tau = 0$ and $\tau = 1$. Two recent studies of channel flows with impermeable hydrophobic walls (Lauga & Cossu 2005; Min & Kim 2005) found that the presence of slip at the walls tends to increase the linear stability of channel flows.

To gain more insight, figure 7(*d*) illustrates the behaviour of the critical Reynolds number (solid line) and the laminar interface velocity (dashed line) in the range $-1 < \tau < 1$ for constant $\sigma = 0.005$, $\varepsilon = 0.6$, and $h_p = h$. The critical Reynolds number reaches a minimum of 1718.15 at $\tau = 0.3$. Note that while the critical Reynolds number increases markedly in the region $0.3 < \tau < 1$, it is comparatively less sensitive to τ in the range $-1 < \tau < 0.3$. One possible explanation for this behaviour is that the presence of a normal velocity at the interface is generally destabilizing, while the presence of a tangential velocity at the interface is generally stabilizing. In the range $-1 < \tau < 0.3$, the destabilizing effects of the normal interface velocity dominate, while in the range $0.3 < \tau < 1$ the destabilizing effects of the normal interface velocity are mitigated by the increasing tangential interface velocity, illustrated in figure 7(*d*) as a dashed line. We expect that the full physical mechanism is more complicated, however, because the Reynolds number does not increase monotonically with τ.

6.3. *The effects of varying h_p on linear stability*

To characterize how the linear stability results are affected when the half-height of the porous layers, h_p, is varied in relation to the half-height of the channel region, h, we repeated the analysis of § 6.1 for $h_p = 2h$, h, $0.5h$, and $0.25h$, maintaining constant $\varepsilon = 0.6$ and $\tau = 0$. Figures 8(*a*) and 8(*b*) illustrate the Orr–Sommerfeld spectra computed using $\sigma_{max} = 0.02$, $Re = 3000$, $\alpha = 1$, $\beta = 0$, and $h_p = 0.25h$ and $2h$, respectively. Comparing the two figures we first note that the eigenvalues labelled 1 and 2 in figure 8(*a*) for the case $h_p = 0.25h$ are less unstable than the corresponding eigenvalues in figure 8(*b*) for the case $h_p = 2h$. Secondly, we note that the porous modes in figure 8(*b*) for the case $h_p = 2h$ are more densely packed along a nearly vertical line. Hence, as expected, the ensemble of the porous modes behaves more like a continuous spectrum as the height of the porous regions increases in relation to the channel height.

Figure 8(*c*) illustrates the critical Reynolds numbers computed in the range $0.0002 \leqslant \sigma \leqslant 0.02$. The Reynolds numbers computed using $h_p = h$ (solid line) and $h_p = 2h$ (dotted line) are visually indistinguishable, while the Reynolds numbers computed using $h_p = 0.5h$ (dash-dotted line) and $h_p = 0.25h$ (dashed line) are increasingly more stable. In order to explain the increase in linear stability with decreasing h_p, we analyse the structure of the eigenfunction, $\widetilde{v}$, of the most unstable mode. Figure 8(*d*) compares the eigenfunction, $\widetilde{v}$, of the least stable eigenvalue, labelled 1 in figures 8(*a*) and 8(*b*), using both $h_p = h$ and $h_p = 0.25h$, while maintaining $Re = 3000$, $\alpha = 1$, and $\beta = 0$ constant. Since $\widetilde{v}$ is generally complex, we simplify the plot by only illustrating the magnitudes, $|\widetilde{v}|$, which have been scaled so that the maximum centreline value is unity. From figure 8(*d*), we see that decreasing h_p in

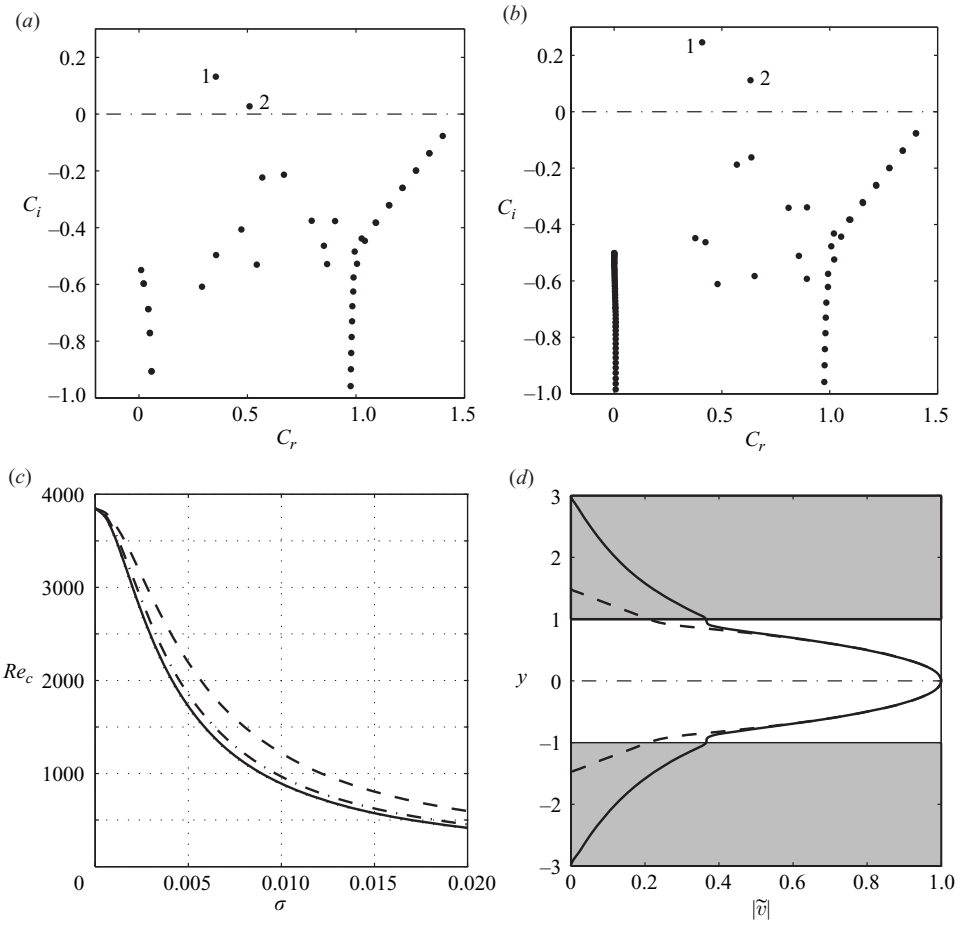

FIGURE 8. For the parameters $\varepsilon = 0.6$, $\tau = 0$, and $\beta = 0$: (*a*) the Orr–Sommerfeld spectrum for $\sigma_{max} = 0.02$, $Re = 3000$, $\alpha = 1$, and $h_p = 0.25h$; (*b*) the Orr–Sommerfeld spectrum for $\sigma_{max} = 0.02$, $Re = 3000$, $\alpha = 1$, and $h_p = 2h$; (*c*) the critical Reynolds number vs permeability, σ, for $h_p = 2h$ (dotted line), h (solid line), $0.5h$ (dash-dotted line), and $0.25h$ (dashed line); (*d*) the eigenfunction magnitude, $|\widetilde{v}|$, of the least stable Orr–Sommerfeld mode for $\sigma = 0.02$, $Re = 3000$, $\alpha = 1$, and $h_p = h$ (solid line) and $0.25h$ (dashed line).

relation to h decreases the amplitude of wall-normal perturbations at the interfaces. This suggests that the destabilizing effects of wall permeability may be largely due to the presence of a non-zero normal perturbation velocity on the surface of a porous wall. Decreasing h_p in relation to h thus diminishes the destabilizing effects of wall permeability by decreasing the wall-normal perturbation velocity at the interfaces. On the other hand, if h_p increases to the point that perturbations naturally diminish to zero before reaching the impermeable walls, further increasing h_p has little or no effect on the linear stability. This explains why the results for $h_p = h$ and $h_p = 2h$ in figure 8(*c*) are visually indistinguishable.

6.4. *The validity of ignoring inertial effects*

Now that we have performed the linear stability analysis by neglecting inertial effects in the porous regions, we can use our results to test the validity of setting the maximum permissible laminar interface velocity to 5 % U_m. When inertial effects are

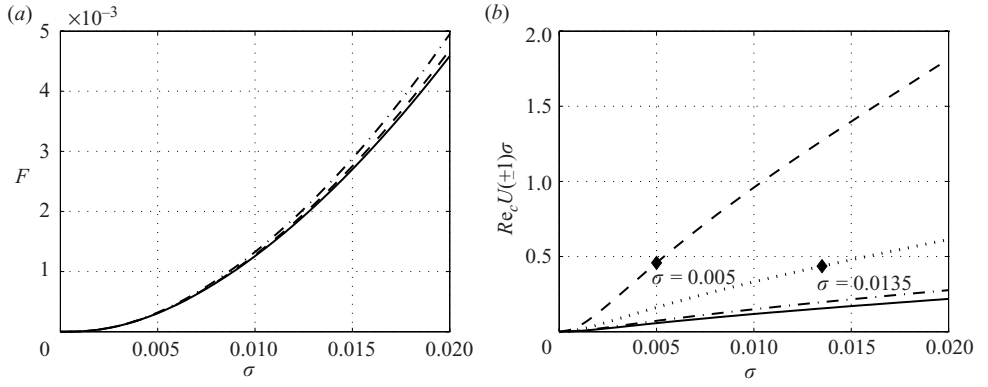

FIGURE 9. (*a*) The behaviour of F as σ increases from σ_{min} to σ_{max} using the parameters $\varepsilon = 0.6$, $h_p = h$, and $\tau = -1.0$ (dashed line), 0.0 (solid line), and 1.0 (dash-dotted line). (*b*) The behaviour of the term $Re_c U(\pm 1)\sigma$ as σ increases from σ_{min} to σ_{max} using the parameters $\varepsilon = 0.6$, $h_p = h$, and $\tau = -1.0$ (solid line), -0.5 (dash-dotted line), 0.5 (dotted line), 1.0 (dashed line). The solid diamonds mark the permeabilities at which the laminar interface velocities have a value close to 5 % U_m.

important in the porous regions, the momentum equation (4.3) must be augmented by the Forchheimer drag term,

$$\frac{1}{\varepsilon_j}\frac{\partial \langle \boldsymbol{v}_j \rangle}{\partial t} = -\nabla \langle p_j \rangle^f + \frac{\nabla^2 \langle \boldsymbol{v}_j \rangle}{\varepsilon_j Re} - \frac{\langle \boldsymbol{v}_j \rangle}{\sigma_j^2 Re} - \frac{\boldsymbol{F}_j \cdot \langle \boldsymbol{v}_j \rangle}{\sigma_j^2 Re}, \quad j = 1, 2. \tag{6.1}$$

It is important to realize that the Forchheimer term affects not only the perturbation equations but also the following equation governing the laminar velocity profiles, $\langle U_j \rangle$, in the porous regions of a channel with two identical porous walls,

$$0 = -\frac{\mathrm{d}P}{\mathrm{d}x} + \frac{1}{\varepsilon Re}\frac{\mathrm{d}^2 \langle U_j \rangle}{\mathrm{d}y^2} - \frac{\langle U_j \rangle}{\sigma^2 Re} - \frac{F \langle U_j \rangle}{\sigma^2 Re}, \quad j = 1, 2, \tag{6.2}$$

where F is a scalar. Even though the laminar profiles in the porous regions are macroscopically uniform, there is a nonlinear drag due to inertial effects occurring on the scale of the pores. Note from equation (6.2) that F can be written as the ratio of the Forchheimer drag term, $F\langle U_j \rangle/(\sigma^2 Re)$, to the Darcy drag term, $\langle U_j \rangle/(\sigma^2 Re)$. Hence, inertial effects are negligible in the porous regions when $F \ll 1$.

In a porous medium of packed granular material, F may be estimated, using a modified form of the Ergun equation (see Macdonald, El-Sayed & Dullien 1979; Whitaker 1996) as

$$F = \frac{Re \langle U_j \rangle d}{100(1-\varepsilon)\varepsilon}, \quad j = 1, 2, \tag{6.3}$$

where $d = \sigma(1-\varepsilon)\sqrt{180/\varepsilon^3}$ is an average grain diameter. Using the critical Reynolds numbers illustrated in figure 7(*b*) for $\varepsilon = 0.6$ and $\tau = -1$, 0, 1, we estimate F for a particular permeability, σ, using the laminar Darcy velocity. Figure 9(*a*) illustrates that for $0 \leqslant \sigma \leqslant 0.02$ and $-1 \leqslant \tau \leqslant 1$, F always remains less than 0.005. Note, however, that equation (6.3) is not valid in the transition layers near the interfaces.

While the Forchheimer drag may be negligible in the porous regions outside the transition layers, inertial effects may still be important near the interfaces. To estimate the importance of inertial effects near the interfaces, we use the momentum transfer

τ	σ	Re_c
-1	0.0085	1059.79
-0.05	0.007	1278.09
0.5	0.0035	2242.58
1	0.0015	3095.29

TABLE 2. For $\varepsilon = 0.6$, $h_p = h$, and $\tau = -1$, -0.5, 0.5, and 1: the maximum permeabilities, σ, and corresponding critical Reynolds numbers for which $Re_c U(\pm 1)\sigma < 0.1$.

conditions of Ochoa-Tapia & Whitaker (1998) which include inertial effects. For the laminar velocity profile in a channel with two identical porous walls, these conditions reduce to

$$U = \langle U_j \rangle, \quad j = 1, 2, \tag{6.4}$$

and

$$\frac{1}{\varepsilon}\frac{\mathrm{d}\langle U_j \rangle}{\mathrm{d}y} - \frac{\mathrm{d}U}{\mathrm{d}y} = \mp\left(\frac{\tau}{\sigma}U + \gamma Re U^2\right), \quad j = 1, 2, \tag{6.5}$$

where γ, which accounts for the effects of inertia in the momentum transfer process, is a dimensionless coefficient of order one that must be determined experimentally (Ochoa-Tapia & Whitaker 1998).

The effects of inertia in the momentum transfer process may be neglected when γ is found experimentally to be zero, or when the ratio of the two terms on the the right-hand side of (6.5), $\gamma Re U(\pm 1)\sigma/\tau$, is much less than one. Because there are currently no published experimental data for γ, we assume that the ratio γ/τ is of order one and we estimate the importance of inertial effects in the interface region using $\gamma Re U(\pm 1)\sigma/\tau \approx Re_c U(\pm 1)\sigma$, where Re_c is the critical Reynolds number. We calculated the critical Reynolds number in a channel with two identical porous walls using the parameters $0.0002 \leqslant \sigma \leqslant 0.2$, $\varepsilon = 0.6$, $\tau = -1$, -0.5, 0.5, and 1, and $h_p = h$, and observed that $Re_c U(\pm 1)\sigma$ increases with both σ and τ as illustrated in figure 9(*b*). Note that we do not report results for $\tau = 0$ as this requires that γ is also zero, in which case inertial effects can be neglected. For $\tau = -1$, $Re_c U(\pm 1)\sigma$ is always less than 0.25; however, for $\tau = 1$, $Re_c U(\pm 1)\sigma$ is already close to the value 0.5 when $\sigma = 0.005$, and is approaching the value 2 when $\sigma = \sigma_{max}$. The permeabilities $\sigma = 0.005$ and $\sigma = 0.0135$ at which the laminar interface velocities for $\tau = 0.5$ and 1 are on the order of 5 % U_m, respectively, are marked with diamonds in figure 9(*b*).

Figure 9 illustrates that it is possible to neglect inertial effects in the porous regions when the Forchheimer term and $\gamma Re U(\pm 1)\sigma/\tau$ are both small with respect to unity. Due to a lack of experimental data for γ and τ, an exact permeability at which inertial effects become non-negligible is not known; however, it is not sufficient for the laminar interface velocity to be less than 5% U_m, unless of course $\gamma = 0$. If instead we required $Re_c U(\pm 1)\sigma < 0.1$, table 2 illustrates the maximum-allowable permeability and corresponding critical Reynolds number for $h_p = h$, $\varepsilon = 0.6$ and $\tau = -1$, -0.5, 0.5, and 1.

To the best of our knowledge, due to the complexity of the governing equations and interface conditions, there are currently no published linear stability analyses of coupled channel and porous flows which include inertial effects in the porous regions. The above analysis is the first which illustrates that it is possible to neglect inertial effects at very small permeabilities and that these permeabilities significantly destabilize channel flow. Because we can only roughly estimate when inertial effects

become important, we will continue using the criterion that the laminar interface velocity must be less than 5 % U_m with the understanding that this limit may be too generous for some porous materials. It is important to understand, however, that in fluid flows through porous media, there is generally no exact permeability or volume-averaged velocity for which inertial effects suddenly become important. Rather, experiments have shown that the effects of inertia tend to increase gradually with increasing permeability and volume-averaged velocity (Costa *et al.* 1999). Consequently, we do not expect our results to become suddenly unreliable as the interface velocity becomes greater than 5% U_m. Also note that because the Reynolds number is small in the pores of a porous medium of small permeability, transition to turbulence is unlikely to occur there.

6.5. *Linear stability results for foametal and aloxite*

To gain more insight into how a real porous material may affect the stability of a channel flow, we fit the parameters ε and τ so that the porous material we model behaves like foametal and aloxite, two porous materials used in the experiments of Beavers & Joseph (1967). Beavers and Joseph proposed the following interface condition, given below in dimensional form, which couples a fully developed laminar channel flow to an adjacent porous flow governed by Darcy's law,

$$\frac{\mathrm{d}u}{\mathrm{d}y} = \frac{\alpha_{BJ}}{\sqrt{k}}(u_{slip} - \langle u \rangle). \tag{6.6}$$

Note that the Beavers and Joseph interface condition (6.6) produces a discontinuous slip velocity, u_{slip}, at the interface. The volume-averaged velocity, $\langle u \rangle$, on the porous side of the interface is given by Darcy's law, while the slip velocity, u_{slip}, on the channel side is given by $\mathrm{d}u/\mathrm{d}y$ and the dimensionless constant α_{BJ} which accounts for the momentum transfer at the interface. Beavers and Joseph determined α_{BJ} experimentally for aloxite and three different foametals, labelled A, B, and C, using a channel with an impermeable upper wall and a lower wall made of the porous material. For each porous material, Beavers and Joseph varied the channel height and measured the fractional increase in flow in the channel region, Φ, caused by the presence of the porous wall,

$$\Phi = \frac{u_m - u_m^*}{u_m^*}, \tag{6.7}$$

where u_m and u_m^* are the mean velocities in a channel with a permeable lower wall and an impermeable upper wall and a channel with two impermeable walls, respectively. The coefficient α_{BJ} was then determined by comparing the experimental results for Φ with those predicted using the interface condition (6.6),

$$\Phi_{BJ} = 3\sigma \left(\frac{1 + \sigma\alpha_{BJ}}{\sigma + 2\alpha_{BJ}} \right). \tag{6.8}$$

The interface conditions of Ochoa-Tapia & Whitaker (1995*a*) predict a fractional increase in flow of

$$\Phi_{OTW} = 3\sigma \left(\frac{1 + \sigma/\sqrt{\varepsilon}}{\sigma - 2\tau + 2/\sqrt{\varepsilon}} \right). \tag{6.9}$$

Because Beavers and Joseph did not report the porosities of their materials, we model the behaviour of foametal A ($\alpha_{BJ} = 0.78$) and aloxite ($\alpha_{BJ} = 0.1$) by assuming a reasonable porosity, ε, and then finding the corresponding coefficient, τ, which produces the best match between the Φ predicted by equations (6.8) and (6.9).

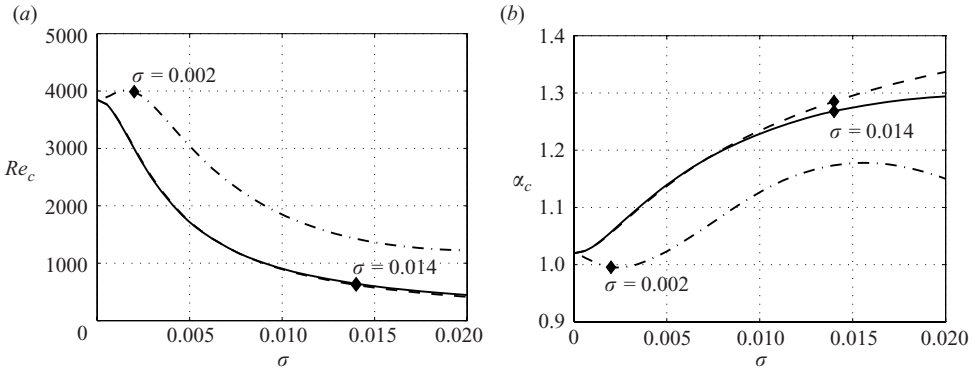

FIGURE 10. The behaviour of (a) the critical Reynolds number, Re_c, and (b) critical wave number, α_c, as the permeability, σ, is varied from $\sigma_{min} = 0.0002$ to $\sigma_{max} = 0.02$ in a channel with two identical porous walls of half-height $h_p = h$ made of foametal A (solid line, $\varepsilon = 0.4$ and $\tau = 0.7$; dashed line, $\varepsilon = 0.95$ and $\tau = 0.194$) or aloxite (dash-dotted line, $\varepsilon = 0.4$ and $\tau = 1.47$). Solid diamonds mark the permeabilities at which the laminar interface velocities, $U(\pm 1)$, have a value close to 5% U_m.

Ochoa-Tapia & Whitaker (1995b) have already determined τ for these materials using an arbitrary porosity of 0.4.

Figures 10(a) and 10(b) illustrate the stability characteristics of a channel with two identical porous walls of half-height $h_p = h$ made of either foametal A ($\varepsilon = 0.4$, $\tau = 0.7$, solid line) or aloxite ($\varepsilon = 0.4$, $\tau = 1.47$, dash-dotted line). The porosities, ε, and interface coefficients, τ, are those determined by Ochoa-Tapia & Whitaker (1995b). Because foametals typically have very high porosities, figures 10(a) and 10(b) also illustrate the stability results for foametal A using a high porosity, $\varepsilon = 0.95$, for which we found that $\tau = 0.194$ provided the best fit to the experiments of Beavers & Joseph (1967). Comparing the results for foametal A generated using $\varepsilon = 0.4$ (solid line) with those generated using $\varepsilon = 0.95$, we note that the results for the critical Reynolds number are visually indistinguishable, while those for the critical wavenumber differ slightly at permeabilities above 0.01. Note that in a channel with walls made of foametal A, the laminar interface velocity is on the order of 5% U_m when $\sigma = 0.014$, while in a channel with walls made of aloxite, this occurs at $\sigma = 0.002$. In figure 10, these permeabilities are marked with solid diamonds.

The results for foametal A are very similar qualitatively to the results presented in § 6.1 for $\varepsilon = 0.6$ and $\tau = 0$, while the results for aloxite are considerably different. In figure 10(a), the critical Reynolds number for aloxite tends, unexpectedly, to increase for small permeabilities in the range $\sigma = [0, 0.0015]$ and thereafter begins to drop. We believe that the increase in critical Reynolds number at very small permeabilities is due to the considerable tangential velocity at the interface, due to the large interface coefficient τ, and the strong resistance to flow normal to the interface, due to the Darcy drag. In effect, for small permeabilities in the range $\sigma = [0, 0.0015]$, the aloxite interface behaves like an impermeable hydrophobic or slip surface which has been shown by Lauga & Cossu (2005) and Min & Kim (2005) to increase linear stability.

7. Linear stability results for skewed laminar velocity profiles

We now consider the linear stability of skewed laminar velocity profiles in channels with a permeable lower wall and an impermeable upper wall. To allow comparison

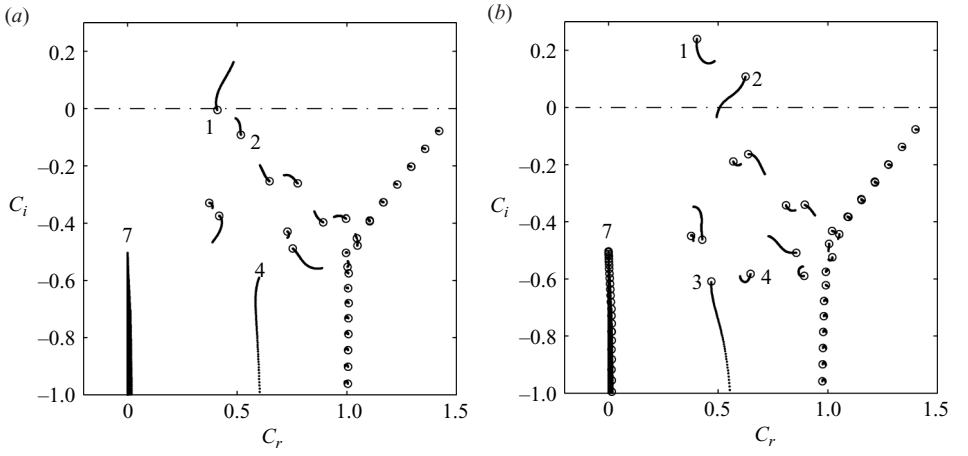

FIGURE 11. (*a*) The trajectory of the Orr–Sommerfeld eigenvalues for $Re = 3000$, $\alpha = 1$, and $\beta = 0$, in a channel with an impermeable upper wall and a porous lower wall with constant $\varepsilon_1 = 0.6$, $\tau_1 = 0$, and $h_1 = h$ as σ_1 is increased from $\sigma_{min} = 0.0002$ (circled) to $\sigma_{max} = 0.02$. (*b*) The trajectory of the Orr–Sommerfeld eigenvalues for $Re = 3000$, $\alpha = 1$, and $\beta = 0$ in a channel with two porous walls with constant $\varepsilon_1 = \varepsilon_2 = 0.6$, $\tau_1 = \tau_2 = 0$, $h_1 = h_2 = h$, and $\sigma_1 = 0.02$ as σ_2 is decreased from $\sigma_{max} = 0.02$ (circled) to $\sigma_{min} = 0.0002$.

with the results presented in § 6.1 for a channel with two identical porous walls, we begin by fixing the parameters $\varepsilon_1 = 0.6$, $\tau_1 = 0$, $h_1 = h$, and vary the permeability σ_1 from $\sigma_{min} = 0.0002$ to $\sigma_{max} = 0.02$.

Figure 11(*a*) illustrates the trajectory of the Orr–Sommerfeld eigenvalues as the permeability is varied from σ_{min} to σ_{max}, while holding $Re = 3000$, $\alpha = 1$, and $\beta = 0$ constant. The eigenvalues corresponding to σ_{min} are circled and are within three decimal places of the eigenvalues associated with a corresponding channel flow with impermeable walls. To gain more insight, the circled eigenvalues in figure 11(*b*) represent the Orr–Sommerfeld spectrum for a channel flow with two porous walls using the parameters $\sigma_1 = \sigma_2 = 0.02$, $\varepsilon_1 = \varepsilon_2 = 0.6$, $\tau_1 = \tau_2 = 0$, and $h_1 = h_2 = h$. The solid lines illustrate the trajectory of these eigenvalues as the permeability of the upper wall, σ_2, is gradually reduced to $\sigma_{min} = 0.0002$.

Comparing figure 11(*a*) to figure 5(*a*), we note that the wall modes are less affected in the case of a channel with only one porous wall. While two wall modes become unstable in the channel with two porous walls, only the mode labelled 1 in figure 11(*a*) becomes unstable in the channel with one porous wall. In figure 11(*b*), we see that as the permeability σ_2 is reduced to σ_{min} in a channel with two porous walls, the unstable wall mode labelled 1 becomes less unstable and the unstable wall mode labelled 2 is stabilized.

In a channel with two porous walls, permeability is responsible for two new wall modes, labelled 3 and 4 in figure 5(*a*). In a channel with only one porous wall, however, permeability is responsible for only one new wall mode, labelled 4 in Figure 11(*a*). In figure 11(*b*), we see that as σ_2 is reduced to σ_{min}, the mode labelled 3, which has a symmetric eigenfunction in the case of a channel with two identical porous walls, is suppressed, while the mode labelled 4, which has an antisymmetric eigenfunction in the case of a channel with two identical porous walls, is significantly less affected. We also note that while symmetry and asymmetry of the eigenfunctions are preserved in

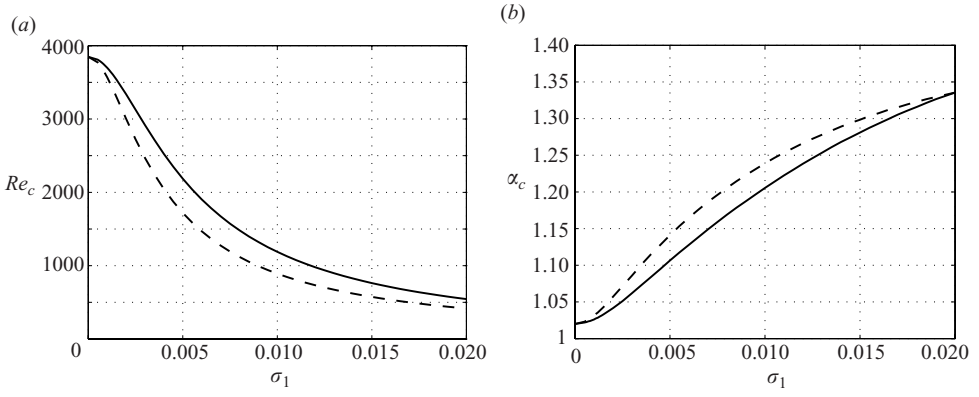

FIGURE 12. A comparison of (*a*) the critical Reynolds number, Re_c, and (*b*) critical wavenumber, α_c, in a channel with two porous walls (dashed line, $\varepsilon = 0.6$, $\tau = 0$, $h_p = h$, $0.0002 \leqslant \sigma \leqslant 0.02$) and a channel with only one porous wall (solid line, $\varepsilon_1 = 0.6$, $\tau_1 = 0$, $h_1 = h$, $0.0002 \leqslant \sigma_1 \leqslant 0.02$).

a channel with two identical porous walls, symmetry is broken in a channel with only one porous wall and the eigenfunctions are all skewed toward the porous interface.

The trajectories of the porous modes labelled with a 7 in figures 11(*a*) and 11(*b*) are not easy to distinguish. We have observed, however, that in a channel with only one porous wall, the porous modes no longer occur in repeated pairs. Because the upper porous wall has been removed, it is no longer physically possible to have a pair of symmetric and antisymmetric eigenfunctions, $\tilde{v}$, associated with each pair of repeated eigenvalues.

Figures 12(*a*) and 12(*b*) illustrate the stability characteristics of a channel with an impermeable upper wall and a porous lower wall characterized by the parameters $\varepsilon_1 = 0.6$, $\tau_1 = 0$, and $h_1 = h$, and allow for a comparison with the results illustrated in figure 7 for a channel with two porous walls. The critical Reynolds number and wavenumber in the channel with only one porous wall are less affected by permeability than in a channel with two porous walls. At a permeability of $\sigma = 0.005$, the critical Reynolds number in the channel with two porous walls is 1719.60, while in the channel with only one porous wall it is 2185.77. This may be due to the stabilizing effect of the impermeable boundary conditions imposed at $y = 1$, and it may also be due to the fact that asymmetric laminar velocity profiles tend to be linearly more stable than symmetric velocity profiles, provided they do not have an inflection point (Fu & Joseph 1970). Note, however, that for the small permeabilities considered in this study, the laminar interface velocity is small and the profile is only slightly skewed toward the lower wall.

Figures 13(*a*) and 13(*b*) compare our numerical results with the numerical and experimental results of Sparrow *et al.* (1973). In those experiments, the critical Reynolds number was measured in a channel with an impermeable upper wall and a porous lower wall for a range of non-dimensional permeabilities, σ_1, by varying the channel half-height. Sparrow *et al.* used a foametal, different from those used by Beavers & Joseph (1967), as a porous material. We model their porous material by assuming a porosity of 0.95 and find that $\tau = 0.878$ provides the best fit to their Beavers and Joseph interface coefficient, $\alpha_{BJ} = 0.146$. For this combination of porosity and interface coefficient, the laminar interface velocity grows quickly with permeability. The permeability at which the laminar interface velocity is nearly 5%

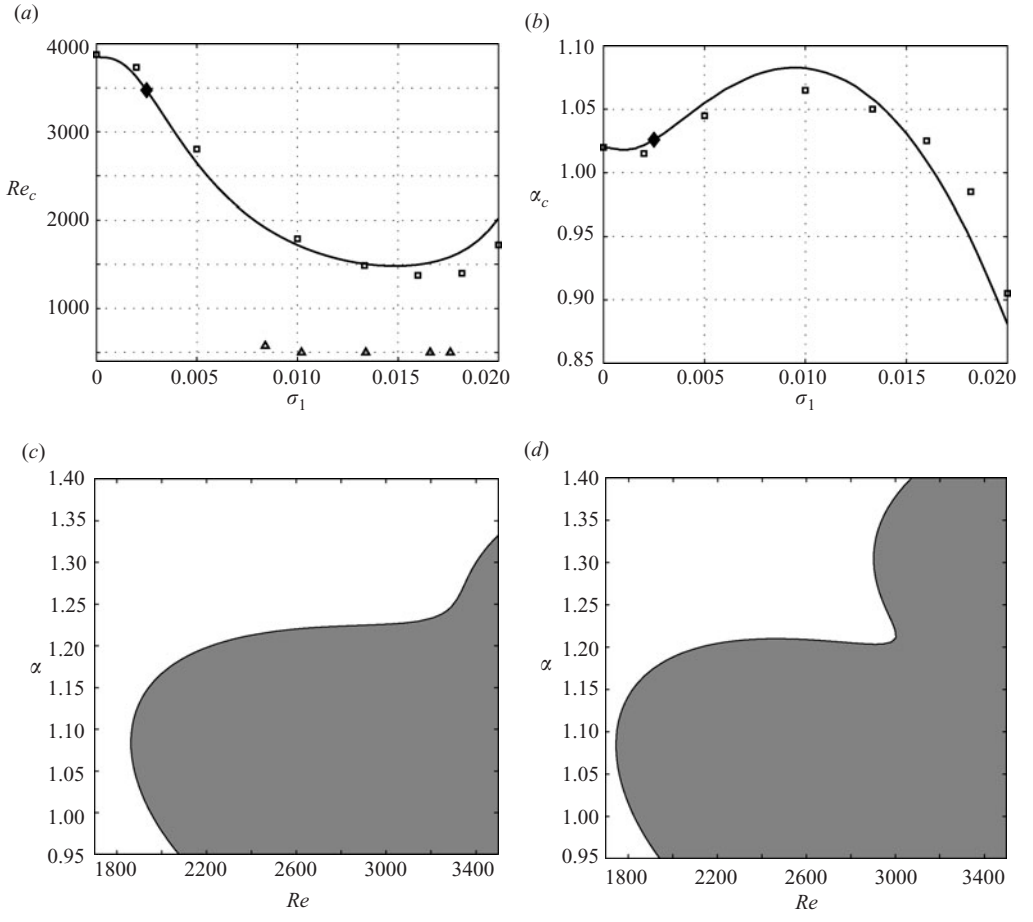

FIGURE 13. For the parameters $\varepsilon_1 = 0.95$, $\tau_1 = 0.878$, and $h_p = h$: (*a*) and (*b*) show a comparison between the current study (solid line) and the numerical (squares) and experimental (triangles) results of Sparrow *et al.* (1973); (*c*) and (*d*) illustrate the neutral stability curves and shaded unstable regions for permeabilities $\sigma_1 = 0.009$ and $\sigma_1 = 0.01$, respectively.

U_m, $\sigma_1 = 0.0025$, is marked with a diamond. Figures 13(*a*) and 13(*b*) illustrate that our numerical results are consistent with those of Sparrow *et al.* and that therefore the approaches of Beavers & Joseph (1967) and Ochoa-Tapia & Whitaker (1995*a*) produce very similar results for the critical Reynolds number and wavenumber. Unfortunately, because Sparrow *et al.* (1973) did not publish spectra or eigenfunctions, we cannot compare the two methods further. The main advantage of the approach of Ochoa-Tapia & Whitaker (1995*a*) is that it should more accurately predict the shape of the eigenfunctions in the porous regions. It is also a first step towards investigating the stability of flows in the presence of interfaces with high-permeability porous materials in which inertial effects are non-negligible.

Note that the numerical results of both Sparrow *et al.* (1973) and the current study predict significantly higher critical Reynolds numbers than those which Sparrow *et al.* observed experimentally. The discrepancy between the numerical results of these studies and the experimental results of Sparrow *et al.* (1973) could be due to the compounding of several factors. First of all, it is well established that even in

channels with impermeable walls, the critical Reynolds number predicted by linear theory is generally significantly higher than the Reynolds number which is observed experimentally. Secondly, neither Sparrow *et al.* nor this study include inertial effects in the porous region. The permeabilities, however, at which Sparrow *et al.* experimentally measured the critical Reynolds numbers are out of the range of our assumptions due to the large laminar interface velocity. Lastly, the porous interface may be more rough than an impermeable wall and thus promote an earlier transition to turbulence.

It is interesting to note that around the permeability $\sigma_1 = 0.009$, for which the laminar interface velocity is about 16 % U_m, a fold begins to form and quickly deepen in the neutral stability curve, as illustrated in figures 13(*c*) and 13(*d*). Similar curves have been observed previously by Chang *et al.* (2006) at similarly high laminar interface velocities. The validity of these folds is doubtful, however, as we have only observed them for large laminar interface velocities which violate our assumption of negligible inertial effects in the porous regions. It is also interesting to note that at permeabilities above $\sigma_1 = 0.015$, the laminar interface velocity is more than 25 % U_m. The resulting skewed laminar profile has a significant stabilizing effect which causes the critical Reynolds number to increase at permeabilities above $\sigma_1 = 0.015$.

In order to asses the validity of the neutral curves presented in figures 13(*c*) and 13(*d*), we carefully analysed the work of Chang *et al.* (2006). Chang *et al.* (2006) recently considered the linear stability of a channel flow with an impermeable upper wall and a porous lower wall using the same analytical formulation as Sparrow *et al.* (1973): the Navier–Stokes and continuity equations in the channel region, Darcy's law and the continuity equation in the porous region, and the Beavers and Joseph condition at the interface. Peculiarly, while Chang *et al.* (2006) non-dimensionalized the governing equations in the channel region using the channel height, $2h$, and the maximum laminar velocity, U_{max}, they simultaneously non-dimensionalized the governing equations in the lower porous region using the height of the porous region, $2h_1$, and the Darcy velocity, $\langle u \rangle = -k_1(\mathrm{d}p/\mathrm{d}x)/\mu$. As a result, they non-dimensionalized the permeability, k_1, using the height of the porous region, obtaining $\sigma_{ch} = \sqrt{k_1}/2h_1$. Note that unlike our definition of the non-dimensionalized permeability, $\sigma_1 = \sqrt{k_1}/h$, the ratio σ_{ch} no longer represents a ratio between a length scale characterizing the permeable material, $\sqrt{k_1}$, and a length scale characterizing the channel region, h. Chang *et al.* (2006) then arbitrarily fixed the non-dimensionalized permeability, $\sigma_{ch} = 0.001$, the porosity, $\varepsilon_1 = 0.3$, and the Beavers and Joseph interface coefficient, $\alpha_{BJ} = 0.1$, and varied the ratio of the channel height to the height of the porous region, $\hat{d} = h/h_1$, between 0.1 and 0.3.

Chang *et al.* (2006) found that the linear stability of their problem was extremely sensitive to the parameter $\hat{d}$, especially near the value $\hat{d} = 0.12$ where they observed that the neutral curve became bi- and even tri-modal. The result that the linear stability of their problem is very sensitive to a change in the parameter $\hat{d}$ when the porous layer is roughly 8 times thicker than the channel region disagrees with our physically rational result. In fact, as discussed in § 6.3, the perturbations tend naturally to diminish in the porous region, and the boundary conditions applied at the external extremities of the porous layer have a diminishing influence on the linear stability of the problem as the height of the porous layer increases. Note, however, that by using two different non-dimensionalizations for the porous and channel regions, Chang *et al.* (2006) are not fixing permeability and only varying the height ratio $\hat{d}$ as they claim. It can be shown that for $\sigma_{ch} = 0.001$ and $0.1 \leqslant \hat{d} \leqslant 0.3$, our definition of the non-dimensionalized permeability varies between 0.0067 and 0.02. The resulting laminar interface velocity, $U(-1)$, varies between 17.5 % U_m and 43.2 % U_m. Despite

the large laminar interface velocity, Chang *et al.* (2006) do not account for inertial effects in their analysis, and consequently, their results are questionable. Also note that their resulting critical Reynolds numbers are generally larger than the corresponding value for a channel flow with impermeable walls because their laminar profiles are significantly skewed.

8. Conclusion

This study considers the three-dimensional linear stability of a laminar flow in a channel with porous walls. The flow in the channel region is governed by the Navier–Stokes and continuity equations, while the flow in the porous regions is governed by volume-averaged forms of the Navier–Stokes and continuity equations derived by Whitaker (1996). The flows in the channel and porous regions are coupled by the momentum transfer conditions of Ochoa-Tapia & Whitaker (1995*a*). Because the momentum transfer conditions are extremely complex when inertial effects are important, we simplify the problem by considering flows for which the inertial effects in the porous regions can be neglected.

At the interfaces between the channel and the porous walls, there is a tangential and normal velocity due to the exchange of momentum between the flow in the channel and the flow in the porous regions. We found that the presence of a normal velocity at the interfaces has a strong destabilizing effect. The presence of a tangential velocity, on the other hand, has a stabilizing effect which has been observed previously in studies of hydrophobic surfaces (Lauga & Cossu 2005; Min & Kim 2005). We performed a parametric study by varying the permeability, interface coefficient τ, and height of the porous regions and characterized their effects on the linear stability of symmetric laminar velocity profiles in channels with two identical porous walls as well as skewed laminar velocity profiles in channels with only one porous wall. We summarize our conclusions for symmetric laminar velocity profiles in § 8.1 and our conclusions for skewed laminar velocity profiles in § 8.2.

8.1. *Linear stability of symmetric laminar velocity profiles*

In channels with two identical porous walls, permeability significantly affects the Orr–Sommerfeld spectrum in comparison with the spectrum associated with channel flow with impermeable walls. Within our assumptions, permeability can destabilize up to two wall modes and introduces a new pair of symmetric and antisymmetric damped wall modes on the left branch of the Orr–Sommerfeld spectrum. Permeability also introduces a new class of damped modes, which we refer to as porous modes, which lie on a near-vertical line and have phase speeds that are nearly zero. We also note that the porous modes approximate a continuous spectrum as the height of the porous layers tends to infinity, $h_p \to \infty$.

Permeability also introduces a new class of porous modes in the Squire spectrum. We do not, however, observe any new wall modes and also find that permeability has a negligible effect on the pre-existing Squire modes. We conclude that the Squire modes remain damped and that Squire's theorem remains valid for all the permeabilities considered in this study.

We validate our results for small permeabilities by setting the permeability of both walls to zero in order to recover the linear stability of a channel flow with impermeable walls. We found that small amounts of wall-permeability, corresponding to a laminar interface velocity on the order of only 1 % of the mean channel velocity, can decrease the linear stability of channel flows dramatically with respect to channel

flows with impermeable walls. As permeability increases, the region of instability in the (Re, α) parameter space becomes substantially larger. The front of the neutral curve becomes more blunt and the number of unstable wavenumbers increases accordingly. The critical Reynolds number is most sensitive to small permeabilities where it experiences its sharpest drop. At higher permeabilities, the critical Reynolds number becomes increasingly less sensitive to permeability and we speculate that it could asymptote to values on the order of 10 % the critical Reynolds number associated with channel flows with impermeable walls. We also observed that the critical wavenumber and phase speed tend to increase with permeability.

We found that increasing the interface coefficient, τ, for a fixed permeability, σ, increases the critical Reynolds number. We speculate that this stabilizing effect is due to the fact that the tangential interface velocity of the laminar velocity profile and the tangential perturbations increases with τ. In selected cases, when τ is large so that there is a significant tangential velocity at the interface, and the permeability is very small so that the normal velocity at the interface is very small, we find that the porous interfaces behave like hydrophobic, or slip, surfaces, causing the critical Reynolds number to increase with respect to its corresponding value for a channel with impermeable walls.

We found that decreasing the half-height, h_p, of the porous regions, in relation to the channel half-height, h, has a stabilizing effect because it diminishes the amplitude of the wall-normal perturbations, $\tilde{v}$, at the interfaces. Conversely, we found that increasing h_p has a destabilizing effect. As h_p increases, however, eventually the end effects at the impermeable walls become negligible and further increasing h_p has no effect.

Using the critical Reynolds numbers we computed, we tested our assumption of negligible inertial effects in the porous regions. We found that inertial effects can be neglected in the porous regions when the Forchheimer coefficient, F, and the product $\gamma_j ReU(\pm 1)\sigma/\tau_j$ are both small with respect to unity.

8.2. *Linear stability of skewed laminar velocity profiles*

Within our assumptions, in channels with only one porous wall, we only observed one wall mode of the Orr–Sommerfeld spectrum to be destabilized by permeability. We also observed that permeability only introduced one new wall mode, which is similar in structure to the new antisymmetric wall mode observed in the linear stability of channels with two porous walls. We draw the conclusion that the non-symmetric geometry of the channel with only one porous wall suppresses the new symmetric mode that is observed in the Orr–Sommerfeld spectra of symmetric laminar velocity profiles. As was observed in the case of a channel with two porous walls, permeability again introduces a new class of porous modes associated with the porous region.

Qualitatively, the trends of the critical Reynolds number and critical wavenumber for a channel with only one porous wall are similar to the trends for a channel with two porous walls; however, the critical Reynolds number and critical wavenumber are noticeably less affected by permeability in the case of a channel with only one porous wall. We speculate that this is due to the stabilizing effects of the boundary conditions at the impermeable wall and the skewness of the laminar profile. We found that the numerical results of this study are consistent with the numerical results of Sparrow *et al.* (1973) and that both numerical results predict significantly higher critical Reynolds numbers than those which Sparrow *et al.* (1973) observed experimentally. The permeabilities, however, at which the critical Reynolds numbers were measured experimentally are out of the range of our assumptions.

Funding was provided by NSERC under a Canada Graduate Scholarship and under Contract No. RGPIN217169.

Appendix. The bounded laminar velocity profile

The non-dimensionalized laminar velocity profile in a channel delimited by parallel, rigid, homogeneous, isotropic, porous layers sealed by impermeable walls at $y = \pm (1 + 2h_j/h)$ is given by

$$U = 3\frac{y^2 + Qy + R}{1 + 3R} \tag{A 1}$$

in the channel region, and

$$\langle U_1 \rangle = \frac{3}{1+3R}\left[\left(\frac{LH_2 + E_2M}{E_1E_2 + H_1H_2}\right)\left(\mathrm{e}^{\sqrt{\varepsilon_1}(2+4l_1+y)/\sigma_1} - \mathrm{e}^{-y\sqrt{\varepsilon_1}/\sigma_1}\right) + 2\sigma_1^2\left(\mathrm{e}^{\sqrt{\varepsilon_1}(1+2l_1+y)/\sigma_1} - 1\right)\right] \tag{A 2}$$

and

$$\langle U_2 \rangle = \frac{3}{1+3R}\left[\left(\frac{E_1L - MH_1}{E_1E_2 + H_1H_2}\right)\left(-\mathrm{e}^{\sqrt{\varepsilon_2}(y-2-4l_2)/\sigma_2} + \mathrm{e}^{-y\sqrt{\varepsilon_2}/\sigma_2}\right) + 2\sigma_2^2\left(\mathrm{e}^{\sqrt{\varepsilon_2}(y-1-2l_2)/\sigma_2} - 1\right)\right] \tag{A 3}$$

in the porous regions, where $l_j = h_j/h$, $j = 1, 2$,

$$Q = \frac{E_1E_2(M + L + F_2 - F_1) + H_1H_2(F_2 - F_1) + E_1LH_2 - E_2MH_1}{E_1E_2 + H_1H_2}, \tag{A 4}$$

$$R = \frac{E_1E_2(L - M + F1 + F2 - 1) + H_1H_2(F_1 + F_2 - 1) - E_1LH_2 - E_2MH_1}{E_1E_2 + H_1H_2}, \tag{A 5}$$

$$L = \mathrm{e}^{2l_1\sqrt{\varepsilon_1}/\sigma_1}\left(\frac{2\sigma_1}{\sqrt{\varepsilon_1}} + \sigma_1^2 - 2\tau_1\sigma_1\right) + 2 - \sigma_1^2 + 2\tau_1\sigma_1 - F_2, \tag{A 6}$$

$$M = \mathrm{e}^{-2l_2\sqrt{\varepsilon_2}/\sigma_2}\left(\frac{2\sigma_2}{\sqrt{\varepsilon_2}} - \sigma_2^2 + 2\tau_2\sigma_2\right) - 2 + \sigma_2^2 - 2\tau_2\sigma_2 + F_1, \tag{A 7}$$

$$F_j = \sigma_j^2\left(\mathrm{e}^{\mp 2l_j\sqrt{\varepsilon_j}/\sigma_j} - 1\right), \quad j = 1, 2, \tag{A 8}$$

$$H_j = \mp E_j\left(1 - 2\frac{\tau_j}{\sigma_j}\right) - \frac{1}{\sqrt{\varepsilon_j}\sigma_1}\left(\mathrm{e}^{\mp\sqrt{\varepsilon_j}(1+4l_j)/\sigma_j} + \mathrm{e}^{\mp\sqrt{\varepsilon_j}/\sigma_j}\right), \quad j = 1, 2, \tag{A 9}$$

and

$$E_j = \frac{1}{2}\left(-\mathrm{e}^{\mp\sqrt{\varepsilon_j}(1+hl_j)/\sigma_1} + \mathrm{e}^{\mp\sqrt{\varepsilon_j}/\sigma_j}\right), \quad j = 1, 2. \tag{A 10}$$

REFERENCES

Alazmi, B. & Vafai, K. 2001 Analysis of fluid flow and heat transfer interfacial conditions between a porous medium and a fluid layer. *Intl J. Heat Mass Transfer* **44**, 1735–1749.

Beavers, G. S. & Joseph, D. D. 1967 Boundary conditions at a naturally permeable wall. *J. Fluid Mech.* **30**, 197–207.

Beavers, G. S., Sparrow, E. M. & Magnuson, R. A. 1970 Experiments on coupled parallel flows in a channel and a bounding porous medium. *J. Basic Engng* (*Trans. ASME*) **92**, 843–848.

Beavers, G. S., Sparrow, E. M. & Rodenz, D. E. 1973 Influence of bed size on the flow characteristics and porosity of randomly packed beds of spheres. *J. Appl. Mech.* **40**, 655–660.

Berkowitz, B. 2002 Characterizing flow and transport in fractured geological media: A review. *Adv. Water Resour.* **25**, 861–884.

Berman, A. S. 1953 Laminar flow in channels with porous walls. *J. Appl. Phys.* **24**, 1232–1235.

Chandesris, M. & Jamet, D. 2006 Boundary conditions at a planar fluid-porous interface for a Poiseuille flow. *Intl J. Heat Mass Transfer* **49**, 2137–2150.

Chang, M., Chen, F. & Straughan, B. 2006 Instability of Poiseuille flow in a fluid overlying a porous layer. *J. Fluid Mech.* **564**, 287–303.

Chang, H. N., Ha, J. S., Park, J. K., Kim, I. H. & Shin, H. D. 1989 Velocity field of pulsatile flow in a porous tube. *J. Biomechanics* **22**, 1257–1262.

Costa, U. M. S., Andrade J. S., Makse, H. A. & Stanley, H. E. 1999 The role of inertia on fluid flow through disordered porous media. *Physica* A **266**, 420–424.

Fu, T. S. & Joseph, D. D. 1970 Linear instability of asymmetric flow in channels. *Phys. Fluids* **13**, 217–221.

Giorgi, T. 1997 Derivation of the Forchheimer law via matched asymptotic expansions. *Transp. Porous Media* **29**, 191–206.

Goharzadeh, A., Khalili, A. & Jørgensen, B. B. 2005 Transition layer thickness at a fluid-porous interface. *Phys. Fluids* **17**, 057102.

Goyeau, B., Lhuillier, D., Gobin, D. & Velarde, M. G. 2003 Momentum transport at a fluid-porous interface. *Intl J. Heat Mass Transfer* **46**, 4071–4081.

Hsu, C. T. & Cheng, P. 1990 Thermal dispersion in a porous medium. *Intl J. Heat Mass Transfer* **33**, 1587–1597.

Jiang, P., Yu, L., Sun, J. & Wang, J. 2004 Experimental and numerical investigation of convection heat transfer in transpiration cooling. *Appl. Thermal Engng* **24**, 1271–1289.

Joseph, D. D., Nield, D. A. & Papanicolaou, G. 1982 Nonlinear equation governing flow in a saturated porous medium. *Water Resour. Res.* **18**, 1049–1052.

Joslin, R. D. 1998 Aircraft laminar flow control. *Annu. Rev. Fluid Mech.* **30**, 1–29.

Kim, J. 2003 Control of turbulent boundary layers. *Phys. Fluids* **15**, 1093–1105.

Lage, J. L. 1998 The fundamental theory of flow through permeable media from Darcy to turbulence. In *Transport Phenomena in Porous Media* (ed. D. B. Ingham & I. Pop), pp. 1–30. Pergamon.

Lauga, E. & Cossu, C. 2005 A note on the stability of slip channel flows. *Phys. Fluids* **17**, 088106.

Macdonald I. F., El-Sayed, M. S. & Dullien F. A. L. 1979 Flow through porous media: The Ergun equation revisited. *Ind. Engng Chem. Fundam.* **18**, 199–208.

Majdalani, J., Zhou, C. & Dawson, C. A. 2002 Two-dimensional viscous flow between slowly expanding or contracting walls with weak permeability. *J. Biomechanics* **35**, 1399–1403.

Min, T. & Kim, J. 2005 Effects of hydrophobic surface on stability and transition. *Phys. Fluids* **17**, 108106.

Nassehi, V. 1998 Modelling of combined Navier Stokes and Darcy flows in crossflow membrane filtration. *Chem. Engng Sci.* **53**, 1253–1265.

Ochoa-Tapia, J. A. & Whitaker, S. 1995*a* Momentum transfer at the boundary between a porous medium and a homogeneous fluid I. Theoretical development. *Intl J. Heat Mass Transfer* **38**, 2635–2646.

Ochoa-Tapia, J. A. & Whitaker, S. 1995*b* Momentum transfer at the boundary between a porous medium and a homogeneous fluid II. Comparison with experiment. *Intl J. Heat Mass Transfer* **38**, 2647–2655.

Ochoa-Tapia, J. A. & Whitaker, S. 1998 Momentum jump condition at a boundary between a porous medium and a homogeneous fluid: Inertial effects. *J. Porous Media* **1**, 201–217.

Sahraoui, M. & Kaviany, M. 1992 Slip and no-slip velocity boundary conditions at the interface of porous, plain media. *Intl J. Heat Mass Transfer* **35**, 927–943.

Schlichting H. & Gersten K. 2000 *Boundary Layer Theory*. Springer.

Schmid, P. J. & Henningson, D. S. 2001 *Stability and Transition in Shear Flows*. Springer.

Shavit, U., Rosenzweig, R. & Assouline, S. 2004 Free flow at the interface of porous surfaces: A generalization of the Taylor brush configuration. *Transp. Porous Media* **54**, 345–360.

Sparrow, E. M., Beavers, G. S., Chen, T. S. & Lloyd, J. R. 1973 Breakdown of the laminar flow regime in permeable-walled ducts. *J. Appl. Mech.* **40**, 337–342.

Tilton, N. & Cortelezzi, L. 2006 The destabilizing effects of wall permeability in channel flows: A linear stability analysis. *Phys. Fluids* **18**, 051702.

Vafai, K. & Tien, C. L. 1981 Boundary and inertia effects on flow and heat transfer in porous media. *Intl J. Heat Mass Transfer* **24**, 195–203.

Whitaker, S. 1986 Flow in porous media I: A theoretical derivation of Darcy's law. *Transp. Porous Media* **1**, 3–25.

Whitaker, S. 1996 The Forchheimer equation: A theoretical development. *Transp. Porous Media* **25**, 27–61.